

Locally stationary spatio-temporal interpolation of Argo profiling float data

Mikael Kuusela

`mkuusela@email.unc.edu`

Statistical and Applied Mathematical Sciences Institute

and

Department of Statistics and Operations Research,

University of North Carolina at Chapel Hill

Michael L. Stein

`stein@galton.uchicago.edu`

Department of Statistics,

University of Chicago

Abstract

Argo floats measure sea water temperature and salinity in the upper 2,000 m of the global ocean. The statistical analysis of the resulting spatio-temporal dataset is challenging due to its nonstationary structure and large size. We propose mapping these data using locally stationary Gaussian process regression where covariance parameter estimation and spatio-temporal prediction are carried out in a moving-window fashion. This yields computationally tractable nonstationary anomaly fields without the need to explicitly model the nonstationary covariance structure. We also investigate Student- t distributed microscale variation as a means to account for non-Gaussian heavy tails in Argo data. We use cross-validation to study the point prediction and uncertainty quantification performance of the proposed approach. We demonstrate clear improvements in the point predictions and show that accounting for the nonstationarity and non-Gaussianity is crucial for obtaining well-calibrated uncertainties. The approach also provides data-driven local estimates of the spatial and temporal dependence scales which are of scientific interest in their own right.

Keywords: Moving-window Gaussian process regression, local kriging, nonstationarity, non-Gaussianity, climatology, physical oceanography

1 Introduction

Subsurface open ocean has traditionally been one of the least studied places on Earth, due to a lack of observational data at fine enough spatial and temporal resolutions. That changed dramatically roughly a decade ago with the introduction of the Argo array of profiling floats. Argo is a collection of nearly 4,000 autonomous floats that measure temperature and salinity in the upper 2,000 m of the ocean. The array's nearly uniform $3^\circ \times 3^\circ \times 10$ days sampling of the global ocean has enabled oceanographers to study the subsurface ocean at unprecedented accuracy and scale. Argo data have been used, for example, to quantify global changes in the

ocean heat content [1], to study ocean circulation [2], mesoscale eddies [3], internal waves [4] and tropical cyclones [5] and to improve climate model predictions [6]. Argo has now become the primary source of subsurface temperature and salinity data for these and hundreds of other studies of ocean climate and dynamics.

A significant portion of scientific results from Argo rely on spatially and temporally interpolated temperature and salinity maps, such as those in [7, 8, 9]. These data products transform the irregularly located Argo observations into a fine regular grid which facilitates further scientific analysis. In a sense, the goal is to “fill in the gaps” between the in-situ Argo observations, such as those shown in Figure 1, and to turn them into a continuously interpolated field in both space and time. To achieve this, a number of statistical modeling assumptions need to be made and the resulting interpolated maps, along with their uncertainties, may be sensitive to these choices. Given the unique nature of Argo data and the scientists’ reliance on the gridded maps, it is of utmost importance to produce the interpolations using the most appropriate statistical techniques and to rigorously understand their performance and limitations.

From the statistical perspective, Argo observations constitute a fascinatingly rich geostatistical dataset. There is a huge volume of data (more than 1.6 million profiles, each having between 50–1,000 vertical observations, have been collected to date), the data are nonstationary in both their mean and covariance structure and exhibit heavy tails and other non-Gaussian features. Argo is also a rare example of a truly four-dimensional ($3 \times \text{space} + \text{time}$) in-situ observational dataset. Due to their cubic computational scaling and typical assumptions of stationarity and Gaussianity, classical geostatistical interpolation techniques, as reviewed for example in [10], cannot directly handle datasets of this size and complexity.

In this paper, we propose a statistical framework for interpolating Argo data that is aimed at addressing both the computational issues caused by the size of the dataset and the modeling challenges caused by the nonstationarity of these data. The approach is based on the basic idea that if a prediction is desired at the spatio-temporal location (\mathbf{x}^*, t^*) , where $\mathbf{x}^* = [x_{\text{lat}}^*, x_{\text{lon}}^*]^T$ is the spatial location in degrees of latitude and longitude and t^* is time, then the observations that are close to (\mathbf{x}^*, t^*) in the (\mathbf{x}, t) space should be the most informative for making the prediction. Indeed, a data point in, say, Northern Atlantic in February is of little value in predicting temperatures in Southern Pacific in August. Furthermore, while it is clear from a simple exploratory inspection of Argo data that a global random field model for the ocean would need to be nonstationary, it is reasonable to assume that the data can be *locally* modeled as a stationary random field. (Assuming that the mean has been successfully removed, a spatio-temporal random field $f(\mathbf{x}, t)$ is stationary if the covariance $k(\mathbf{x}_1, t_1, \mathbf{x}_2, t_2) = \text{Cov}(f(\mathbf{x}_1, t_1), f(\mathbf{x}_2, t_2))$ is a function of $(\mathbf{x}_1 - \mathbf{x}_2, t_1 - t_2)$ only, $k(\mathbf{x}_1, t_1, \mathbf{x}_2, t_2) = k(\mathbf{x}_1 - \mathbf{x}_2, t_1 - t_2)$.) We combine these two ideas by considering data only within a small spatio-temporal neighborhood of (\mathbf{x}^*, t^*) and by assuming that this subset of data can be modeled as a stationary random field. We use the data within the neighborhood to first estimate the unknown parameters of the random field model using maximum likelihood and then to perform the interpolation. As first proposed by Haas in [11, 12], we use the neighborhoods in a moving-window fashion: when moving to the next grid point, the window is re-centered and the parameters re-estimated. This leads to locally stationary gridded predictions of the globally nonstationary random field and data-driven local estimates of the globally varying spatio-temporal dependence structure. The approach is computationally efficient since it considers only a subset of the full dataset at a time and since the computations across the grid points can be fully parallelized. In a recent line of work described in [13, 14, 15, 16], a closely related moving-window method has been developed and successfully applied to mapping of satellite observations.

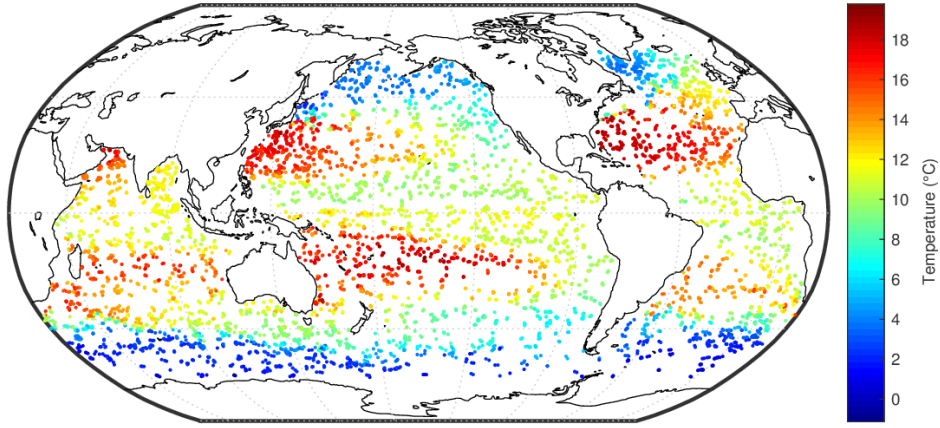


Figure 1: Argo temperature data at 300 db (≈ 300 m) for February 2012. Argo provides in-situ temperature and salinity observations for the upper 2,000 m of the global ocean. The statistical question studied in this work is how to interpolate these irregularly sampled data into a dense regular grid.

The Roemmich–Gilson climatology (along with the associated anomalies) [7] is one of the more popular gridded Argo data products. Roemmich and Gilson first estimate the mean field using a weighted local spatio-temporal regression fit to several years of Argo data and then perform kriging [17, 18] (also known as optimal interpolation [19] or objective analysis/mapping [20] and closely related to Gaussian process regression [21]) on the mean-subtracted monthly residuals to obtain the interpolated anomaly fields. In this work, we use the Roemmich–Gilson mean field, but improve the modeling of the anomalies in three important ways: first, we include time in the interpolation; second, we use data-driven local estimates of the nonstationary covariance structure as described above; and third, we consider Student- t distributed microscale variation (the so-called nugget effect) in order to account for non-Gaussian heavy tails in Argo data. We investigate the point prediction and uncertainty quantification performance of the proposed approach using cross-validation studies. We demonstrate that adding the temporal component to the mapping leads to major performance improvements, while the locally estimated model parameters and the Student nugget are crucial for obtaining reasonable uncertainties. The uncertainty quantification part is particularly important as the Roemmich–Gilson data product does not currently provide any uncertainty information, presumably due to challenges in modeling the nonstationary and non-Gaussian features of the data. Furthermore, our local estimates of the model parameters contain information about ocean dynamics and are of scientific interest in their own right. In fact, even the basic idea of using the observed data to estimate the covariance parameters needed in the mapping appears to be largely unexplored in the oceanographic context. Indeed, most of the existing Argo data products (see Sections 2(b) and 2(c) for a literature review) do not use formal data-driven criteria, such as maximum likelihood, to estimate the model parameters, even though such techniques are standard in the relevant statistics literature [18, 21, 17, 10]. A notable exception is the work described in [2, 22] where ocean velocity fields are mapped based on variogram fits to Argo data.

In the present paper we focus primarily on interpolating Argo temperature anomalies, but similar techniques can be developed for the salinity fields. The rest of this paper is structured as follows: Section 2 provides an overview of Argo and reviews the existing gridded Argo data products with an emphasis on the Roemmich–Gilson climatology. Section 3 explains the proposed locally stationary spatio-temporal interpolation methodology. Section 4 applies the new

approach to Argo data and studies its performance in terms of point predictions, uncertainty quantification and the estimated model parameters. Section 5 concludes and discusses directions for future work.

2 Overview of Argo and existing data products

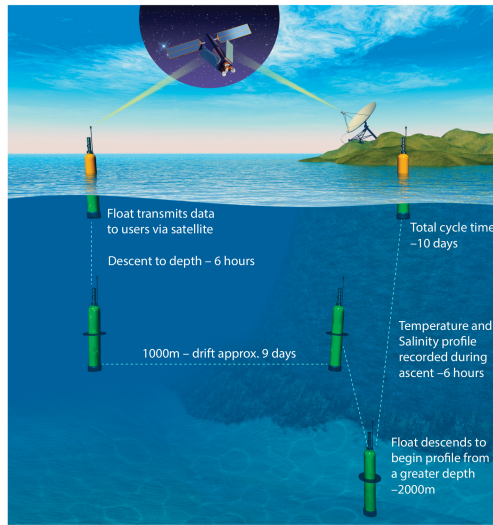
(a) Argo floats and data

Argo [23, 24] is a global array of profiling floats for observing the subsurface ocean. The floats follow a regular cycle to measure temperature (T), salinity (S) and pressure (P) in the upper 2,000 meters of the water column; see Figure 2(a). The cycle starts when a float at the surface changes its buoyancy and descends to the parking depth of 1,000 meters. The float stays at that depth for approximately 9 days. During that time, it does not collect data and simply drifts with the current. After this, the float descends further down to 2,000 meters and turns on its measurement devices. The float then ascends back to the surface recording in-situ temperature, salinity and pressure triplets (T_i, S_i, P_i) along the water column. The end result is a temperature and salinity profile for the upper 2,000 meters of the ocean. Once the float reaches the surface, it obtains a satellite position fix, sends its data via satellite to ground-based data centers and starts a new cycle. Each cycle takes approximately 10 days to complete.

There are currently almost 4,000 Argo floats operating in the world’s oceans. This results in nearly uniform global coverage at roughly $3^\circ \times 3^\circ$ spatial resolution and 10 days temporal resolution. Figure 1 illustrates a monthly aggregate of Argo data at 300 db. (Pressure is measured in *desibars*, db. A pressure change of 1 db is approximately equivalent to a depth change of 1 m.) The first Argo floats were deployed in 1999, sparse global coverage was achieved in 2004 and the $3^\circ \times 3^\circ$ design resolution in 2007. While satellites provide plenty of data of the ocean surface, there are few other sources of data besides Argo for the subsurface ocean. Indeed, the pre-Argo ship-based subsurface temperature and salinity observations are sparse in both space and time with heavy sampling biases towards the Northern Hemisphere, coastal areas and summer months, while Argo provides much larger quantities of data and much more uniform sampling [24]. This improvement is particularly dramatic in the Southern Ocean during winter months, where pre-Argo subsurface data are extremely scarce [7, Figure 1.1].

Argo data are transmitted using either the Argos or Iridium satellite systems. Newer floats (Figure 2(b) shows a SOLO-II float at the Scripps Institution of Oceanography) primarily use Iridium, while roughly a half of the current array uses the older Argos system. The transmission system has some important implications on the quality of Argo data: the limited bandwidth of the Argos system allows these floats to transmit only 50–100 data points per profile, while the Iridium floats can transmit up to a 1,000 observations at a time, leading to a finer vertical resolution. To ensure successful data transmission, the Argos floats need to remain on the surface for 6–12 hours, while Iridium data transmission takes only 15 minutes. This improves the lifetime and decreases the undesired surface drift of the Iridium floats. The Argos floats also rely on the same satellite system for location information, while the Iridium floats use GPS, improving the accuracy of the position data.

The nominal accuracy of Argo temperature, salinity and pressure data are 0.005 °C, 0.01 psu and 2.5 db, respectively [24]. (Salinity is measured in *practical salinity units*, psu.) The temperature data are considered very reliable, but pressure and salinity measurements may need to be adjusted for sensor offsets and drift. Argo data are distributed in two ways: real-time data is made available within 24 hours and has passed through various automatic checks and adjust-



(a) Park and profile cycle



(b) Argo float

Figure 2: Figure (a) shows a schematic of the typical cycle of an Argo float. Most of the time, the float drifts at the 1,000 meters parking depth. Every 10 days, it descends further to 2,000 meters, turns on its sensors and measures a temperature and salinity profile as it ascends to the surface. (Figure courtesy of the Argo Program, <http://www.argo.ucsd.edu>, <http://doi.org/10.17882/42182>, used with permission.) Figure (b) shows an Argo float at the Scripps Institution of Oceanography (SIO). The measurement sensors and an antenna for satellite communications can be seen at the top of the float. The cylindrical part houses batteries, electronics and a hydraulic pump which is used to inflate and deflate an external bladder at the bottom of the float to adjust its buoyancy. There are a few different models of Argo floats. The one shown in the photo is a SOLO-II float designed and built at SIO. (Photo by Mikael Kuusela.)

ments, while delayed-mode data has been manually checked by an oceanographic expert and may contain finer corrections for sensor offsets and drift [25]. Depending on the float model and configuration, the reported temperature and salinity values may be spot samples or pressure-bin averages. The vertical sampling is also often nonuniform, with finer sampling closer to the surface. Some floats also sample at finer temporal resolution than the nominal 10 days, in particular in the Kuroshio region near Japan.

Two extensions of the basic Argo program are currently under development [24]: The Deep Argo program aims to extend the vertical coverage of the Argo array to 6,000 meters, while biogeochemical Argo floats are to be equipped with extra sensors for measuring biogeochemical variables, such as dissolved oxygen, nitrate, chlorophyll and pH. Pilot arrays of both programs have been deployed in certain areas of the ocean.

(b) Roemmich–Gilson climatology

The Roemmich–Gilson (RG) climatology and its anomalies [7, 26] are constructed by first estimating a seasonally varying mean field and then performing kriging on the mean-subtracted monthly residuals. The vertical dimension is handled by binning the profiles into 58 pressure bins, whose size increases with depth. The mean field is estimated using 3 adjacent pressure levels, but the kriging for the anomalies is carried out using data from only one pressure level at a time.

The RG mean field is a weighted local least-squares spatio-temporal regression fit that is carried out separately for each latitude-longitude grid point and each depth level. The regression function is (John Gilson, personal communication, 2016)

$$m(x_{\text{lat}}, x_{\text{lon}}, z, t) = \beta_0 + [\text{first- and second-order terms of } x_{\text{lat}}, x_{\text{lon}} \text{ and } z] \\ + \sum_{k=1}^6 \gamma_k \sin\left(2\pi k \frac{t}{365.25}\right) + \sum_{k=1}^6 \delta_k \cos\left(2\pi k \frac{t}{365.25}\right), \quad (1)$$

where x_{lat} is latitude, x_{lon} is longitude, z is pressure and t is time in days within a year. This function is fitted to $3 \times 12 \times 100$ nearest neighbors, where the factors refer to the 3 depth levels and the 12 calendar months. The nearest neighbors are found across the entire Argo data set and are given weights according to their horizontal distance from the grid point. The horizontal distance metric is

$$d_{\text{RG}}(\mathbf{x}_1, \mathbf{x}_2) = \sqrt{(\Delta x_{\text{lat}})^2 + (\Delta x_{\text{lon}})^2 + \text{Pen}(\mathbf{x}_1, \mathbf{x}_2)^2}, \quad (2)$$

where $\mathbf{x}_i = [x_{\text{lat},i}, x_{\text{lon},i}]^T$, Δx_{lat} is the meridional distance in kilometers, Δx_{lon} is the zonal distance in kilometers (converted from degrees to kilometers using the midpoint latitude) and $\text{Pen}(\mathbf{x}_1, \mathbf{x}_2)$ is a penalty term for crossing ocean depth contours (see [7] for details). Once fitted, the regression function is evaluated at the grid point for the midpoint of each month to produce the monthly mean field estimates for that latitude, longitude and depth.

The anomalies are computed one month at a time. Here the crucial modeling choice concerns the covariance structure of those fields. The Roemmich–Gilson covariance function is

$$k(\mathbf{x}_1, \mathbf{x}_2) \propto 0.77 \exp\left(-\left(\frac{d_{\text{RG},a}(\mathbf{x}_1, \mathbf{x}_2)}{140 \text{ km}}\right)^2\right) + 0.23 \exp\left(-\frac{d_{\text{RG},a}(\mathbf{x}_1, \mathbf{x}_2)}{1111 \text{ km}}\right), \quad (3)$$

where $d_{\text{RG},a}(\mathbf{x}_1, \mathbf{x}_2)$ is otherwise the same distance metric as in Equation (2), but with Δx_{lon} replaced by $a((x_{\text{lat},1} + x_{\text{lat},2})/2) \cdot \Delta x_{\text{lon}}$, where [7, 26]

$$a(x_{\text{lat}}) = \begin{cases} 1, & \text{if } |x_{\text{lat}}| > 20^\circ, \\ \frac{1}{8} + \frac{7}{160^\circ} |x_{\text{lat}}|, & \text{if } |x_{\text{lat}}| \leq 20^\circ. \end{cases} \quad (4)$$

Using $d_{\text{RG},a}(\mathbf{x}_1, \mathbf{x}_2)$ instead of $d_{\text{RG}}(\mathbf{x}_1, \mathbf{x}_2)$ has the effect of elongating the zonal dependence in the tropics. This results in a nonstationary covariance function that varies in the zonal direction depending on the latitude. However, the meridional range is kept constant and the same covariance function is used at all longitudes, all depths, all seasons and for both the temperature and the salinity anomalies. Also the noise-to-signal variance ratio (the ratio of the nugget variance and the Gaussian process variance σ^2/ϕ in the terminology and notation of Section 3) is set to be the constant 0.15 throughout the global ocean.

The functional form and the parameter values in (3) are motivated by the observed empirical correlation of the steric height anomaly (essentially a vertical integral of the density anomaly; see Section 7.6.2 in [27]) in Argo and satellite altimetry data (see Figure 2.2 in [7]). The parameter values are chosen by a graphical comparison of the correlation functions and not through a formal estimation procedure, such as maximum likelihood or weighted least squares. Since the RG covariance function is chosen based on a vertically integrated quantity, it is likely to be sub-optimal for mapping quantities in the mixed layer, which contributes only a little to the vertical integral, but where atmospheric interaction is expected to cause the dependence structure to differ from the deeper ocean.

An important limitation of the Roemmich–Gilson climatology is that it does not provide uncertainty estimates. In principle the formal kriging variance could be used to provide Gaussian prediction intervals, but this would require defining the proportionality constant in Equation (3) (this constant cancels out in the kriging point predictions). Even if this proportionality constant was provided, the uncertainties are unlikely to be reliable given that the RG covariance does not vary with depth and uses a fixed noise-to-signal variance ratio. Another limitation is that the RG covariance is only a function of the spatial locations and does not take the temporal dimension into account.

Gasparin et al. [28] improve the Roemmich–Gilson model by including time in the covariance and adding nonstationarity in the meridional range parameter. They also briefly investigate the prediction uncertainties. But their analysis is limited to the Equatorial Pacific only, their covariance remains the same for all depths and all longitudes and their covariance parameters are not based on formal statistical estimates. In this work, we go further and develop data-driven covariances for Argo temperature data that can vary as a function of latitude, longitude, depth and season. Covariance estimates, anomaly maps and uncertainties are investigated in the global ocean at three exemplary depths. The covariances include time and nonstationarity is allowed in all covariance parameters, including the zonal, meridional and temporal range parameters.

(c) Other Argo data products

Besides the Roemmich–Gilson climatology, several other gridded Argo data products have been produced. We give here a brief overview of some of these products. Our treatment is by no means exhaustive and a full list of Argo data products can be found at http://www.argo.ucsd.edu/Gridded_fields.html.

The defining feature of the MIMOC product [8] is that it is mapped on isopycnals (surfaces of constant density) instead of pressure surfaces. This approach may have distinct advantages in handling the vertical movement of isopycnals and in avoiding density inversions. The EN4 data product [9] provides uncertainty estimates, but its uncertainty quantification procedure seems statistically *ad hoc*, is only validated in the root-mean-square sense and shows signs of miscalibration below approximately 400 m. ISAS [29] and MOAA GPV [30] are further examples of kriging-based Argo data products. For most products, there is some effort to use physical data to justify the chosen covariance parameters but no formal statistical estimators of these parameters are used. An exception is the work of Gray and Riser [2, 22] that uses a weighted least-squares variogram fit and an iteratively estimated mean field to map ocean velocity fields based on Argo data. Out of the data products mentioned here, [7] and [2] use Argo data only, while the other products also incorporate data from other sources.

3 Locally stationary interpolation of Argo data

This section describes the statistical methodology we propose for interpolating Argo temperature data. The approach is based on a locally stationary spatio-temporal Gaussian process (GP) regression model. We start by linearly interpolating the Argo temperature profiles to a given pressure level. We then subtract the Roemmich–Gilson mean field (see Sections 2(b) and 4(a)) and work with the residuals, which are assumed to have zero mean. Our goal is to use these residuals to produce gridded maps of temperature anomalies. Similar to the Roemmich–Gilson climatology, our analysis is carried out separately for each pressure level.

Let (\mathbf{x}^*, t^*) with $\mathbf{x}^* = [x_{\text{lat}}^*, x_{\text{lon}}^*]^T$ be a space-time grid point for which a prediction is desired.

We assume that within a small spatio-temporal neighborhood $\mathcal{W}(\mathbf{x}^*, t^*) = [x_{\text{lat}}^* - x_{\text{win}}, x_{\text{lat}}^* + x_{\text{win}}] \times [x_{\text{lon}}^* - x_{\text{win}}, x_{\text{lon}}^* + x_{\text{win}}] \times [t^* - t_{\text{win}}, t^* + t_{\text{win}}]$ around (\mathbf{x}^*, t^*) the following model holds:

$$y_{i,j} = f_i(\mathbf{x}_{i,j}, t_{i,j}) + \varepsilon_{i,j}, \quad f_i \stackrel{\text{iid}}{\sim} \text{GP}(0, k(\mathbf{x}_1, t_1, \mathbf{x}_2, t_2; \boldsymbol{\theta})), \quad (5)$$

where $i = 1, \dots, n$ refers to years and $j = 1, \dots, m_i$ to observations within $\mathcal{W}(\mathbf{x}^*, t^*)$ at the desired pressure level in the i th year, $y_{i,j}$ is the (i, j) th temperature measurement (with mean removed), $\mathbf{x}_{i,j} = [x_{\text{lat},i,j}, x_{\text{lon},i,j}]^T$ and $t_{i,j}$ are the location (in degrees of latitude and longitude) and time (in days within a year) of $y_{i,j}$ and $\text{GP}(0, k(\mathbf{x}_1, t_1, \mathbf{x}_2, t_2; \boldsymbol{\theta}))$ denotes a zero-mean Gaussian process with a stationary space-time covariance function $k(\mathbf{x}_1, t_1, \mathbf{x}_2, t_2; \boldsymbol{\theta}) = k(\mathbf{x}_1 - \mathbf{x}_2, t_1 - t_2; \boldsymbol{\theta})$ depending on parameters $\boldsymbol{\theta}$. We use the nonseparable anisotropic exponential space-time covariance function $k(\mathbf{x}_1, t_1, \mathbf{x}_2, t_2; \boldsymbol{\theta}) = \phi \exp(-d(\mathbf{x}_1, t_1, \mathbf{x}_2, t_2))$, where the GP variance $\phi > 0$,

$$d(\mathbf{x}_1, t_1, \mathbf{x}_2, t_2) = \sqrt{\left(\frac{x_{\text{lat},1} - x_{\text{lat},2}}{\theta_{\text{lat}}}\right)^2 + \left(\frac{x_{\text{lon},1} - x_{\text{lon},2}}{\theta_{\text{lon}}}\right)^2 + \left(\frac{t_1 - t_2}{\theta_t}\right)^2} \quad (6)$$

and θ_{lat} , θ_{lon} and θ_t are positive range parameters. The nugget effect $\varepsilon_{i,j}$ is independent of f_i and assumed to follow either $\varepsilon_{i,j} \stackrel{\text{iid}}{\sim} N(0, \sigma^2)$, where $N(0, \sigma^2)$ is the zero-mean Gaussian distribution with variance σ^2 , or $\varepsilon_{i,j} \stackrel{\text{iid}}{\sim} t_\nu(\sigma^2)$, where $t_\nu(\sigma^2)$ is the scaled Student- t distribution with $\nu > 1$ degrees of freedom and scale parameter $\sigma > 0$ (that is, $Z \sim t_\nu(\sigma^2)$ if and only if $\frac{Z}{\sigma} \sim t_\nu$, where t_ν is the Student- t distribution with ν degrees of freedom). The Student nugget provides a way to model non-Gaussian heavy tails in Argo data. Notice that under this model we obtain n independent realizations of the random field, one for each year, which facilitates estimating the model parameters.

We employ model (5) in a moving-window fashion: for each grid point (\mathbf{x}^*, t^*) , we use data within the local neighborhood $\mathcal{W}(\mathbf{x}^*, t^*)$ to estimate the model parameters and to predict $y_i^* = f_i(\mathbf{x}^*, t^*) + \varepsilon_i^*$. When we move to the next grid point, we re-center the window around the new location and re-estimate the model parameters. The overlap of the nearby windows results in smoothly varying local estimates of the model parameters. Such moving-window approach to Gaussian process regression was first proposed by Haas in [11, 12]. Figure 3 illustrates the method.

This approach facilitates both the modeling and the computational challenges in Argo data analysis. Instead of having to specify a global nonstationary covariance model, the moving-window approach enables us to handle the nonstationarity in Argo data using an ensemble of locally fitted stationary GP models. In terms of the computations, the approach essentially replaces the inversion of one large covariance matrix by many inversions of smaller covariance matrices. This results in significant computational gains, especially since the computations across the grid points are embarrassingly parallel. More concretely, let n be the number of years and m the typical number of global Argo observations for each year. Then, to leading order, the computing time of a global GP regression fit would be $n \cdot C \cdot m^3$, where C is a constant. When each moving window contains fraction f of data, there are N grid points and the computations are parallelized to p threads, the computing time of the moving-window approach is $\frac{1}{p} \cdot N \cdot n \cdot C \cdot (fm)^3 = \frac{1}{p} \cdot N \cdot f^3 \cdot n \cdot C \cdot m^3$. Rough values for the analysis carried out in this paper are $f = 0.01$, $N = 30,000$ and $p = 30$, leading to a speed-up factor $(\frac{1}{p} \cdot N \cdot f^3)^{-1} = 1,000$.

In model (5), we understand the nugget $\varepsilon_{i,j}$ to primarily reflect ocean variability at spatio-temporal scales smaller than the $3^\circ \times 3^\circ \times 10$ days Argo sampling resolution. The fitted nugget may also capture sensor noise, but we consider this component to be negligibly small in comparison to the microscale ocean variability. This interpretation of the nugget leads us to make

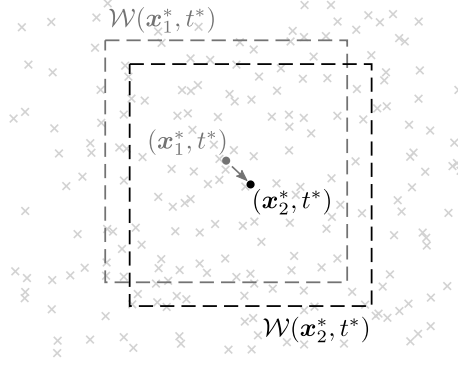


Figure 3: Illustration of moving-window Gaussian process regression. In order to make a prediction at the grid point (\mathbf{x}_1^*, t^*) , data in its local neighborhood $\mathcal{W}(\mathbf{x}_1^*, t^*)$ are used to first estimate the covariance parameters and then to make the prediction. When moving to the next grid point (\mathbf{x}_2^*, t^*) , the window moves along and the parameter estimates and the prediction are made using data in the new local neighborhood $\mathcal{W}(\mathbf{x}_2^*, t^*)$. For ease of graphical presentation, the time axis is suppressed here, but the same concept applies in the full spatio-temporal space.

predictions for $y_i^* = f_i(\mathbf{x}^*, t^*) + \varepsilon_i^*$ instead of $f_i(\mathbf{x}^*, t^*)$, which widens the predictions intervals by an amount corresponding to the microscale component ε_i^* . This is a sensible approach for temperature data, since the microscale ocean temperature variability is orders of magnitude larger than the noise-level of Argo temperature sensors. For salinity, especially at large depth, it would be appropriate to model the measurement process more carefully, but this is outside the scope of the present work.

To demonstrate the importance of proper modeling of temporal effects, we also consider a spatial version of model (5). In that case, the moving window remains the same as before, but we ignore the temporal separation of the observations within the window by dropping the time covariate $t_{i,j}$ in Equation (5). The distance metric for the covariance is given by Equation (6) without the time term. The next two sections explain in detail the parameter estimation, point prediction and uncertainty quantification steps under model (5).

(a) Gaussian nugget

With the Gaussian nugget $\varepsilon_{i,j} \sim N(0, \sigma^2)$, the unknown model parameters are the covariance parameters $\boldsymbol{\theta} = [\phi, \theta_{\text{lat}}, \theta_{\text{lon}}, \theta_t]^T$ and the nugget variance σ^2 . We use maximum likelihood to estimate these parameters from Argo data. For each year $i = 1, \dots, n$, let $\mathbf{K}_i(\boldsymbol{\theta})$ be the $m_i \times m_i$ matrix with elements $[\mathbf{K}_i(\boldsymbol{\theta})]_{j,k} = k(\mathbf{x}_{i,j}, t_{i,j}, \mathbf{x}_{i,k}, t_{i,k}; \boldsymbol{\theta})$ and let \mathbf{y}_i be the column vector with elements $y_{i,j}$, $j = 1, \dots, m_i$. The log-likelihood of the parameters $(\boldsymbol{\theta}, \sigma^2)$ is

$$\ell(\boldsymbol{\theta}, \sigma^2) = \sum_{i=1}^n \log p(\mathbf{y}_i | \boldsymbol{\theta}, \sigma^2) \quad (7)$$

$$= -\frac{1}{2} \sum_{i=1}^n \left[\log \det (\mathbf{K}_i(\boldsymbol{\theta}) + \sigma^2 \mathbf{I}) + \mathbf{y}_i^T (\mathbf{K}_i(\boldsymbol{\theta}) + \sigma^2 \mathbf{I})^{-1} \mathbf{y}_i + m_i \log(2\pi) \right] \quad (8)$$

and the maximum likelihood estimator (MLE) of $(\boldsymbol{\theta}, \sigma^2)$ is

$$(\hat{\boldsymbol{\theta}}, \hat{\sigma}^2) = \arg \max_{(\boldsymbol{\theta}, \sigma^2) \in \mathbb{R}_+^5} \ell(\boldsymbol{\theta}, \sigma^2). \quad (9)$$

The MLE needs to be obtained using numerical optimization; we use the BFGS quasi-Newton algorithm, as implemented in the Matlab Optimization Toolbox R2016a [31], on log-transformed parameters.

We base the predictions on the conditional distribution $p(y_i^*|\mathbf{y}_i, \hat{\boldsymbol{\theta}}, \hat{\sigma}^2)$, where we have plugged in the MLE $(\hat{\boldsymbol{\theta}}, \hat{\sigma}^2)$ for the model parameters. Standard manipulations show that the predictive distribution is

$$(y_i^*|\mathbf{y}_i, \hat{\boldsymbol{\theta}}, \hat{\sigma}^2) \sim N \left((\mathbf{k}_i^*(\hat{\boldsymbol{\theta}}))^T (\mathbf{K}_i(\hat{\boldsymbol{\theta}}) + \hat{\sigma}^2 \mathbf{I})^{-1} \mathbf{y}_i, \hat{\phi} + \hat{\sigma}^2 - (\mathbf{k}_i^*(\hat{\boldsymbol{\theta}}))^T (\mathbf{K}_i(\hat{\boldsymbol{\theta}}) + \hat{\sigma}^2 \mathbf{I})^{-1} \mathbf{k}_i^*(\hat{\boldsymbol{\theta}}) \right), \quad (10)$$

where $\mathbf{k}_i^*(\boldsymbol{\theta})$ is a column vector with elements $k(\mathbf{x}^*, t^*, \mathbf{x}_{i,j}, t_{i,j}; \boldsymbol{\theta})$, $j = 1, \dots, m_i$. We make point predictions using the conditional mean $\hat{y}_i^* = E(y_i^*|\mathbf{y}_i, \hat{\boldsymbol{\theta}}, \hat{\sigma}^2) = (\mathbf{k}_i^*(\hat{\boldsymbol{\theta}}))^T (\mathbf{K}_i(\hat{\boldsymbol{\theta}}) + \hat{\sigma}^2 \mathbf{I})^{-1} \mathbf{y}_i$. This is the well-known kriging predictor (see, e.g., [17, 18]) based on data within the moving window $\mathcal{W}(\mathbf{x}^*, t^*)$ and with plug-in values for the model parameters. It is mean square error optimal assuming that model (5) is correct and ignoring the uncertainty of the model parameters. To quantify the uncertainty of y_i^* , we use the $1 - \alpha$ predictive intervals based on $p(y_i^*|\mathbf{y}_i, \hat{\boldsymbol{\theta}}, \hat{\sigma}^2)$,

$$[\underline{y}_i^*, \bar{y}_i^*] = \left[\hat{y}_i^* - z_{1-\alpha/2} \sqrt{\text{Var}(y_i^*|\mathbf{y}_i, \hat{\boldsymbol{\theta}}, \hat{\sigma}^2)}, \hat{y}_i^* + z_{1-\alpha/2} \sqrt{\text{Var}(y_i^*|\mathbf{y}_i, \hat{\boldsymbol{\theta}}, \hat{\sigma}^2)} \right], \quad (11)$$

where $z_{1-\alpha/2}$ is the $1 - \alpha/2$ standard normal quantile and $\text{Var}(y_i^*|\mathbf{y}_i, \hat{\boldsymbol{\theta}}, \hat{\sigma}^2) = \hat{\phi} + \hat{\sigma}^2 - (\mathbf{k}_i^*(\hat{\boldsymbol{\theta}}))^T (\mathbf{K}_i(\hat{\boldsymbol{\theta}}) + \hat{\sigma}^2 \mathbf{I})^{-1} \mathbf{k}_i^*(\hat{\boldsymbol{\theta}})$ is the kriging variance.

(b) Student nugget

With the Student nugget $\varepsilon_{i,j} \sim t_\nu(\sigma^2)$, the likelihood $p(\mathbf{y}|\boldsymbol{\theta}, \sigma^2, \nu) = \prod_{i=1}^n p(\mathbf{y}_i|\boldsymbol{\theta}, \sigma^2, \nu)$ and the predictive distribution $p(y_i^*|\mathbf{y}_i, \boldsymbol{\theta}, \sigma^2, \nu)$ are not available in closed form. To achieve computationally tractable inferences, we employ the Laplace approximation as in [32]; see also Section 3.4 in [21]. We give here only an overview of the method and refer to [32, 21] for details.

Denoting $\mathbf{f}_i = [f_i(\mathbf{x}_{i,1}, t_{i,1}), \dots, f_i(\mathbf{x}_{i,m_i}, t_{i,m_i})]^T$, the i th year likelihood can be written as

$$p(\mathbf{y}_i|\boldsymbol{\theta}, \sigma^2, \nu) = \int p(\mathbf{y}_i|\mathbf{f}_i, \sigma^2, \nu) p(\mathbf{f}_i|\boldsymbol{\theta}) d\mathbf{f}_i = \int \exp(\Psi_i(\mathbf{f}_i)) d\mathbf{f}_i, \quad (12)$$

where $\Psi_i(\mathbf{f}_i) = \log(p(\mathbf{y}_i|\mathbf{f}_i, \sigma^2, \nu)p(\mathbf{f}_i|\boldsymbol{\theta}))$. Denote the mode of $\Psi_i(\mathbf{f}_i)$ by $\hat{\mathbf{f}}_i$. Since

$$\hat{\mathbf{f}}_i = \arg \max_{\mathbf{f}_i \in \mathbb{R}^{m_i}} \Psi_i(\mathbf{f}_i) = \arg \max_{\mathbf{f}_i \in \mathbb{R}^{m_i}} \{p(\mathbf{y}_i|\mathbf{f}_i, \sigma^2, \nu)p(\mathbf{f}_i|\boldsymbol{\theta})\} \quad (13)$$

$$= \arg \max_{\mathbf{f}_i \in \mathbb{R}^{m_i}} \{p(\mathbf{f}_i|\mathbf{y}_i, \boldsymbol{\theta}, \sigma^2, \nu)p(\mathbf{y}_i|\boldsymbol{\theta}, \sigma^2, \nu)\} = \arg \max_{\mathbf{f}_i \in \mathbb{R}^{m_i}} p(\mathbf{f}_i|\mathbf{y}_i, \boldsymbol{\theta}, \sigma^2, \nu), \quad (14)$$

$\hat{\mathbf{f}}_i$ is also the mode of the conditional distribution $p(\mathbf{f}_i|\mathbf{y}_i, \boldsymbol{\theta}, \sigma^2, \nu)$. Employing a second-order Taylor expansion of $\Psi_i(\mathbf{f}_i)$ around $\hat{\mathbf{f}}_i$,

$$\Psi_i(\mathbf{f}_i) \approx \Psi_i(\hat{\mathbf{f}}_i) - \frac{1}{2}(\mathbf{f}_i - \hat{\mathbf{f}}_i)^T \left(-\frac{\partial^2}{\partial \mathbf{f}_i^2} \Psi_i(\mathbf{f}_i) \Big|_{\mathbf{f}_i = \hat{\mathbf{f}}_i} \right) (\mathbf{f}_i - \hat{\mathbf{f}}_i), \quad (15)$$

Equation (12) becomes a Gaussian integral that can be evaluated analytically. The resulting approximate log-likelihood is [32, 21]

$$\begin{aligned} \log q(\mathbf{y}_i|\boldsymbol{\theta}, \sigma^2, \nu) \\ = \log p(\mathbf{y}_i|\hat{\mathbf{f}}_i, \sigma^2, \nu) - \frac{1}{2} \hat{\mathbf{f}}_i^T \mathbf{K}_i(\boldsymbol{\theta})^{-1} \hat{\mathbf{f}}_i - \frac{1}{2} \log \det \mathbf{K}_i(\boldsymbol{\theta}) - \frac{1}{2} \log \det (\mathbf{K}_i(\boldsymbol{\theta})^{-1} + \mathbf{W}_i(\hat{\mathbf{f}}_i, \sigma^2, \nu)), \end{aligned} \quad (16)$$

where $\mathbf{W}_i(\hat{\mathbf{f}}_i, \sigma^2, \nu) = -\frac{\partial^2}{\partial \mathbf{f}_i^2} \log p(\mathbf{y}_i | \mathbf{f}_i, \sigma^2, \nu) \Big|_{\mathbf{f}_i = \hat{\mathbf{f}}_i}$. The n -year approximate log-likelihood is then the sum of the one-year log-likelihoods, $\log q(\mathbf{y} | \boldsymbol{\theta}, \sigma^2, \nu) = \sum_{i=1}^n \log q(\mathbf{y}_i | \boldsymbol{\theta}, \sigma^2, \nu)$, and this is maximized numerically with respect to the model parameters $(\boldsymbol{\theta}, \sigma^2, \nu)$.

Denote $f_i^* = f_i(\mathbf{x}^*, t^*)$. The predictive distribution for f_i^* is

$$p(f_i^* | \mathbf{y}_i, \hat{\boldsymbol{\theta}}, \hat{\sigma}^2, \hat{\nu}) = \int p(f_i^* | \mathbf{f}_i, \hat{\boldsymbol{\theta}}) p(\mathbf{f}_i | \mathbf{y}_i, \hat{\boldsymbol{\theta}}, \hat{\sigma}^2, \hat{\nu}) d\mathbf{f}_i, \quad (17)$$

where we have plugged in the Laplace approximated MLEs for the model parameters. Here one can again employ the Laplace approximation by taking a second-order Taylor expansion of $\log p(\mathbf{f}_i | \mathbf{y}_i, \hat{\boldsymbol{\theta}}, \hat{\sigma}^2, \hat{\nu})$ around its mode. This results in the Gaussian approximation $(\mathbf{f}_i | \mathbf{y}_i, \hat{\boldsymbol{\theta}}, \hat{\sigma}^2, \hat{\nu}) \stackrel{a}{\sim} N(\hat{\mathbf{f}}_i, (\mathbf{K}_i(\hat{\boldsymbol{\theta}})^{-1} + \mathbf{W}_i(\hat{\mathbf{f}}_i, \hat{\sigma}^2, \hat{\nu}))^{-1})$. Equation (17) then becomes a Gaussian integral, which can be evaluated to give

$$(f_i^* | \mathbf{y}_i, \hat{\boldsymbol{\theta}}, \hat{\sigma}^2, \hat{\nu}) \stackrel{a}{\sim} N\left((\mathbf{k}_i^*(\hat{\boldsymbol{\theta}}))^T \mathbf{K}_i(\hat{\boldsymbol{\theta}})^{-1} \hat{\mathbf{f}}_i, \hat{\phi} - (\mathbf{k}_i^*(\hat{\boldsymbol{\theta}}))^T (\mathbf{K}_i(\hat{\boldsymbol{\theta}}) + \mathbf{W}_i(\hat{\mathbf{f}}_i, \hat{\sigma}^2, \hat{\nu}))^{-1} \mathbf{k}_i^*(\hat{\boldsymbol{\theta}})\right). \quad (18)$$

The Laplace approximated predictive distribution for $y_i^* = f_i^* + \varepsilon_i^*$ is therefore

$$(y_i^* | \mathbf{y}_i, \hat{\boldsymbol{\theta}}, \hat{\sigma}^2, \hat{\nu}) \stackrel{a}{\sim} P_{Z_1 + Z_2}, \quad (19)$$

where $P_{Z_1 + Z_2}$ denotes the distribution of $Z_1 + Z_2$, with Z_1 following the Gaussian distribution in Equation (18), $Z_2 \sim t_{\hat{\nu}}(\hat{\sigma}^2)$ and Z_1 and Z_2 are independent. The point predictions are made using the approximate conditional mean $\hat{y}_i^* = (\mathbf{k}_i^*(\hat{\boldsymbol{\theta}}))^T \mathbf{K}_i(\hat{\boldsymbol{\theta}})^{-1} \hat{\mathbf{f}}_i \approx E(y_i^* | \mathbf{y}_i, \hat{\boldsymbol{\theta}}, \hat{\sigma}^2, \hat{\nu})$ and the $1 - \alpha$ predictive intervals are $[\underline{y}_i^*, \bar{y}_i^*] = [\hat{y}_i^* - q_{1-\alpha/2}, \hat{y}_i^* + q_{1-\alpha/2}]$, where $q_{1-\alpha/2}$ is the $1 - \alpha/2$ quantile of the distribution of $(Z_1 - \hat{y}_i^*) + Z_2$, where Z_1 and Z_2 are as in Equation (19). Since $q_{1-\alpha/2}$ is not available in closed form, we compute it by Monte Carlo sampling.

Software implementations of Gaussian processes with a Student nugget differ in terms of how $\hat{\mathbf{f}}_i = \arg \max_{\mathbf{f}_i \in \mathbb{R}^{m_i}} p(\mathbf{f}_i | \mathbf{y}_i, \boldsymbol{\theta}, \sigma^2, \nu)$ is computed and how the approximate log-likelihood $\log q(\mathbf{y} | \boldsymbol{\theta}, \sigma^2, \nu)$ is maximized. In this work, we compute the Student fits using the GPML toolbox [33, 34], which we have adapted to include the multi-year likelihood and the Student predictive intervals. GPML uses conjugate gradient descent for finding the model parameters $(\boldsymbol{\theta}, \sigma^2, \nu)$ and Newton's method for maximizing $p(\mathbf{f}_i | \mathbf{y}_i, \boldsymbol{\theta}, \sigma^2, \nu)$ with respect to \mathbf{f}_i , with special care for the nonconcavity of the latter problem [33]. When finding the approximate MLEs, we initialize $\boldsymbol{\theta} = [\phi, \theta_{\text{lat}}, \theta_{\text{lon}}, \theta_t]^T$ to the MLEs from the Gaussian nugget fit. This initialization was found to significantly improve the convergence and stability of the conjugate gradient descent.

4 Results

In this section, we study the performance of the statistical methodology described in Section 3 in interpolating Argo temperature data. We use the Roemmich–Gilson approach described in Section 2(b) as a baseline and investigate how data-driven local estimates of the covariance structure improve treatment of the anomalies. Section 4(a) describes the models and datasets that we consider. We then study the fitted models from three perspectives: 1) cross-validated point prediction performance in Section 4(b), 2) cross-validated uncertainty quantification performance in Section 4(c) and 3) the estimated spatio-temporal dependence structure in Section 4(d).

(a) Experiment setup

Our experiments are performed by fitting models to Argo temperature data collected between 2007 and 2016. We investigate three pressure levels, 10 db, 300 db and 1500 db, with the model parameters estimated separately for each pressure level. We focus on 1- and 3-month temporal windows centered around February (i.e., February 2007, February 2008, ..., February 2016 or January–March 2007, January–March 2008, ..., January–March 2016 are considered independent realizations from the statistical model in Equation (5)). To enable comparison of models with different time windows, all the cross-validation studies are done for February data only.

Table 1 describes the different models considered in this study. Model 1, which we regard as the baseline reference model, is our reimplementation of the procedure developed by Roemmich and Gilson [7]; see Section 2(b). Apart from a few technical details (see below), this model is the same as the one used to produce the Roemmich–Gilson Argo climatology and its associated anomalies. Models 2–6 are different variants of the locally stationary mapping procedure described in Section 3. In each case, the mapping is carried out on a $1^\circ \times 1^\circ$ grid and the covariance parameters are estimated using maximum likelihood within a $20^\circ \times 20^\circ$ moving window on this grid. Model 2 is a 1-month fit with a spatial covariance $k(\mathbf{x}_1, \mathbf{x}_2; \boldsymbol{\theta})$ and a Gaussian nugget. Model 3 is otherwise the same but with a Student nugget. Model 4 is a 3-month version of model 2. Models 5 and 6 are 3-month fits with a spatio-temporal covariance $k(\mathbf{x}_1, t_1, \mathbf{x}_2, t_2; \boldsymbol{\theta})$ and either a Gaussian or a Student nugget. The spatio-temporal fits are done with 3 months of data to make sure that there are enough profiles from each float to estimate the temporal covariance structure (there are usually 9 profiles from each float within a 3-month window).

For each model, the mean field is the Roemmich–Gilson local regression fit (see Section 2(b)). The publicly available version of the RG climatology [26] includes only the annual mean field, but John Gilson kindly provided us with the mid-month evaluations of the local mean functions (1). We use either these mid-month evaluations treating the mean as a constant over the temporal period (spatial mean) or alternatively a temporally varying reconstruction of the original mean (spatio-temporal mean) as indicated in Table 1. The temporally varying mean is reconstructed from the 12 mid-month evaluations of (1) by handling the one remaining degree of freedom by finding the minimum-norm solution in the space of the regression coefficients.

The reference model (model 1) captures the key aspects of the Roemmich–Gilson approach. There are however two technical differences between our implementation and theirs. First, we do not include the depth penalty term $\text{Pen}(\mathbf{x}_1, \mathbf{x}_2)$ when we compute the point estimates and

Table 1: Description of the models we consider for interpolating Argo temperature data. Model 1 is a reimplementation of the procedure developed by Roemmich and Gilson (RG) [7] and models 2–6 are variants of locally stationary interpolation. The models differ in terms of how time is taken into account, in the distribution of the microscale variation captured by the nugget effect and in the length of the temporal window used in the fit (see text for more details).

Model	Time window	Mean	Covariance	Nugget
1	February	RG (spatial)	RG-like	Gaussian
2	February	RG (spatial)	Local (spatial)	Gaussian
3	February	RG (spatial)	Local (spatial)	Student
4	January–March	RG (spatial-temporal)	Local (spatial)	Gaussian
5	January–March	RG (spatial-temporal)	Local (spatial-temporal)	Gaussian
6	January–March	RG (spatial-temporal)	Local (spatial-temporal)	Student

the uncertainties. And, second, we do not implement specialized treatment of distances across islands or continental land. These differences are unlikely to markedly affect the conclusions drawn below. Finally, we note that when computing the prediction intervals for the reference model, we need to provide the proportionality constant in Equation (3) (i.e., the variance ϕ of the Gaussian process part of the spatial model). Since Roemmich and Gilson do not provide uncertainty estimates, they also do not have estimates of this constant as it cancels out in the point predictions. To simulate what could have potentially been done to produce uncertainties under the Roemmich–Gilson model, we estimate the proportionality constant using a moving-window empirical variance. That is, the RG-inspired prediction intervals at the grid point \mathbf{x}^* are formed using the covariance model (3) with the following estimate of the GP variance ϕ :

$$\hat{\phi} = \frac{\text{empirical variance of } y_{i,j} \text{ in a } 20^\circ \times 20^\circ \times 1 \text{ month window centered at } \mathbf{x}^*}{1.15}, \quad (20)$$

where the denominator originates from the RG noise-to-signal variance ratio 0.15 via the relation $\text{Var}(y_{i,j}) = \phi + \sigma^2 = \phi \left(1 + \frac{\sigma^2}{\phi}\right) = 1.15 \cdot \phi$. We emphasize that the resulting prediction intervals are not part of the original Roemmich–Gilson climatology and by no means advocated by them for uncertainty quantification.

We fit models 1–6 to the global Argo data set as of May 8, 2017 [35]. The quality control criteria we use for filtering out profiles with technical issues are given in the supplement [36]. There were a total of 1,417,813 Argo profiles in 2007–2016, out of which 994,709 passed our selection criteria. We also perform a further temporal filtering to focus on the desired time windows and a spatial filtering based on the Roemmich–Gilson land mask [26], which filters out profiles located in marginal seas, such as the Mediterranean Sea or the Gulf of Mexico. The final data set has 70,227 profiles in February and 223,797 profiles in January to March.

The analysis was carried out using Matlab R2016a. As described in Section 3(b), we use GPML [33, 34] to fit models 3 and 6, while the other models are our own implementations. The computations were carried out on the Midway2 cluster at the University of Chicago Research Computing Center. The possibility to parallelize the moving-window computations to the 28 threads of the Midway2 compute nodes was crucial for making the analysis computationally feasible. The Matlab code used to produce the results is available on Github [37].

(b) Point predictions

We first investigate the performance of the different models in making point predictions of the temperature field. Figure 4 shows the February 2012 temperature anomalies at 10 db, 300 db and 1500 db for the locally stationary spatio-temporal model with a Gaussian nugget (model 5) and for the reference model (model 1). The maps are on a $1^\circ \times 1^\circ$ grid and the space-time field is evaluated at noon February 15, 2012. The overall patterns in both fields are similar: one can recognize the large-scale anomalies near the surface, the elongated patterns in subsurface Equatorial regions and the meanders and eddies associated with the western boundary currents and the Antarctic Circumpolar Current. There are, however, a number of clear differences between the maps. Especially at 10 db, the reference map shows small speckles that are absent from the locally fitted map. This is related to the Roemmich–Gilson covariance parameters which are not optimized for mapping anomalies near the surface. Also, while present in both maps, the zonal elongation of the anomalies in the Equatorial regions is much more pronounced in the reference maps.

In order to study the difference between the reference method and the locally stationary maps in more quantitative terms, we perform a cross-validation study comparing the predictive

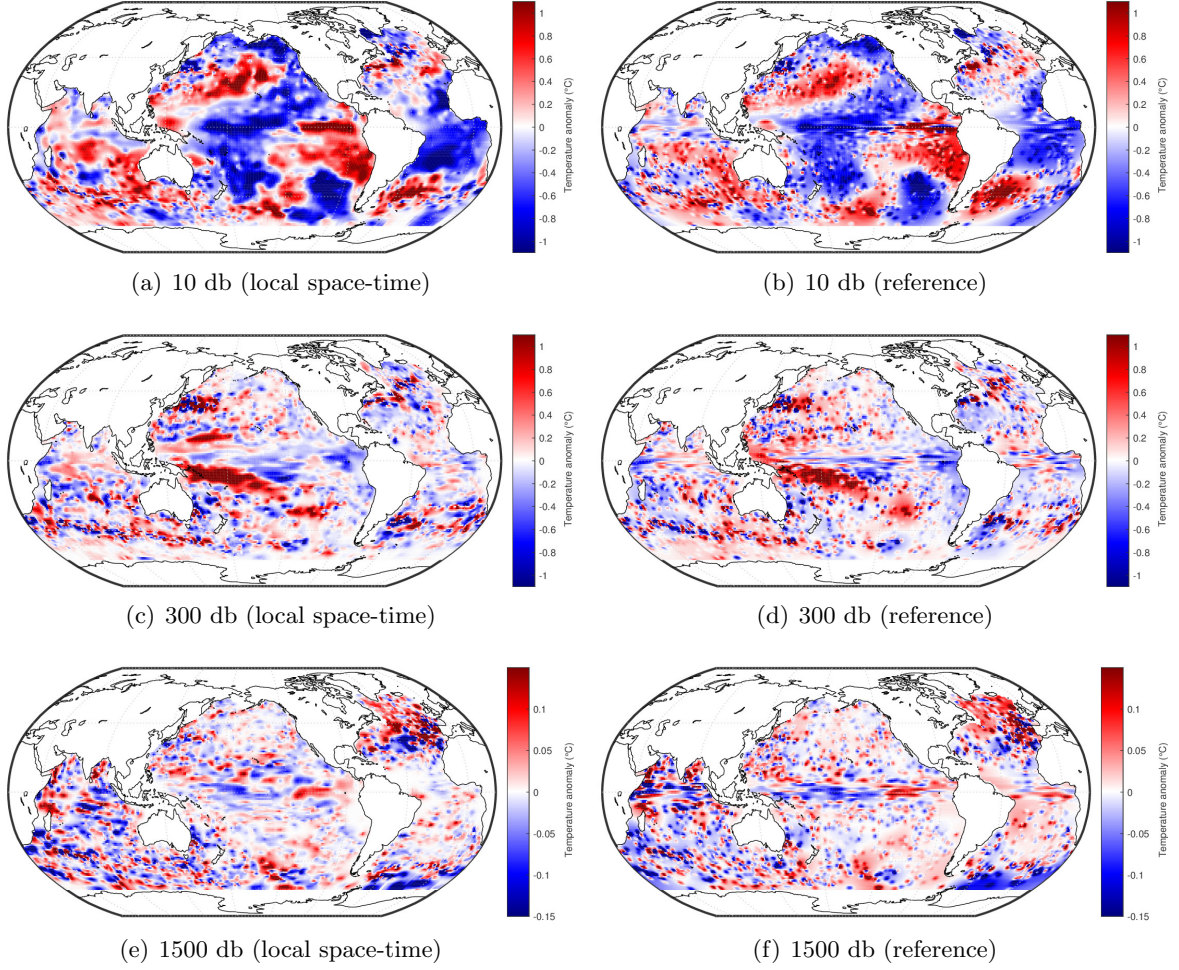


Figure 4: Argo temperature anomalies for February 2012 at 10 db, 300 db and 1500 db for the locally stationary 3-month spatio-temporal model with a Gaussian nugget (model 5, left column) and for the Roemmich–Gilson-like reference model (model 1, right column).

performance of the different methods. We use two cross-validation procedures: in leave-one-observation-out (LOOO) cross-validation we leave out one temperature observation at a time, while in leave-one-float-out (LOFO) cross-validation we leave out an entire float. LOOO predictions are easier to make since there will almost always be nearby observations from the same float to constrain the temperature value at the prediction location. LOFO cross-validation on the other hand creates a “gap” in the Argo array and has a higher amount of irreducible error. In the actual mapping problem, the typical distance from a grid point to nearby floats will be somewhere in between these two extremes.

We investigate the cross-validation performance in terms of the root-mean-square error (RMSE), the median absolute error (MdAE) and the third quartile of the absolute error (Q_3AE). Let $\hat{y}_{-(i,j)}$ be the prediction at $(\mathbf{x}_{i,j}, t_{i,j})$ with either $y_{i,j}$ removed from the dataset (LOOO) or all observations with the same float ID as $y_{i,j}$ removed (LOFO). Then

$$RMSE = \sqrt{\frac{1}{\sum_{i=1}^n m_i} \sum_{i=1}^n \sum_{j=1}^{m_i} (\hat{y}_{-(i,j)} - y_{i,j})^2} \quad (21)$$

Table 2: Point prediction performance measured in terms of the root-mean-square error (RMSE), the third quartile of the absolute error (Q₃AE) and the median absolute error (MdAE) for leave-one-observation-out (LOOO) cross-validation. The compared models are the Roemmich–Gilson spatial mean, the Roemmich–Gilson-like reference model (model 1), the locally stationary 1-month and 3-month spatial models (models 2 and 4) and the locally stationary 3-month spatio-temporal model (model 5), all with a Gaussian nugget. The units are degrees Celsius and the percentages in the parentheses are improvements in comparison to the reference model.

Pressure level	Perf. metric	Spatial mean	Reference model	Space (1 month)	Space (3 months)	Space-time (3 months)
10 db	RMSE	0.8889	0.6135	0.5876 (4.2 %)	0.5667 (7.6 %)	0.5072 (17.3 %)
	Q ₃ AE	0.8670	0.5026	0.4824 (4.0 %)	0.4568 (9.1 %)	0.3735 (25.7 %)
	MdAE	0.4750	0.2556	0.2490 (2.6 %)	0.2293 (10.3 %)	0.1801 (29.5 %)
300 db	RMSE	0.8149	0.5782	0.5692 (1.6 %)	0.5675 (1.9 %)	0.5124 (11.4 %)
	Q ₃ AE	0.6320	0.4213	0.4150 (1.5 %)	0.4005 (4.9 %)	0.3684 (12.6 %)
	MdAE	0.3062	0.1991	0.1957 (1.7 %)	0.1873 (5.9 %)	0.1740 (12.6 %)
1500 db	RMSE	0.1337	0.1014	0.0997 (1.7 %)	0.0935 (7.8 %)	0.0883 (12.9 %)
	Q ₃ AE	0.1043	0.0736	0.0725 (1.5 %)	0.0678 (7.9 %)	0.0641 (12.8 %)
	MdAE	0.0530	0.0356	0.0355 (0.3 %)	0.0328 (8.0 %)	0.0311 (12.7 %)

and MdAE and Q₃AE are the sample median and sample third quartile of $\{|\hat{y}_{-(i,j)} - y_{i,j}|\}$, $i = 1, \dots, n$, $j = 1, \dots, m_i$. When cross-validating $y_{i,j}$, the model parameters are taken from the moving window centered at the $1^\circ \times 1^\circ$ grid point closest to $y_{i,j}$. The parameter estimates and the mean fields are kept fixed during the cross-validation.

Table 2 shows the LOOO cross-validation performance for the models with a Gaussian nugget (models 1, 2, 4 and 5). Also included is the performance when the predictions are made using only the Roemmich–Gilson spatial mean without any modeling of the anomalies (the performance of the spatio-temporal mean is only slightly better and omitted for clarity purposes). For all three pressure levels and for all three performance metrics, the relative performance of the models is in the following order: the reference model (model 1) outperforms the spatial mean, the locally stationary 1-month spatial model (model 2) outperforms the reference model (model 1), the locally stationary 3-month spatial model (model 4) outperforms the 1-month spatial model (model 2) and the locally stationary 3-month spatio-temporal model (model 5) outperforms the 3-month spatial model (model 4). Combining data-driven local covariance parameters with a longer temporal window and a covariance structure that includes the time leads to fairly substantial 10 % – 30 % performance improvements over the reference model. The improvement is particularly large near the surface at 10 db. The distribution of the squared prediction errors (not shown) has a much fatter right tail than it would be if the errors followed a common normal distribution, so we also consider MdAE and Q₃AE as summaries of prediction performance to make sure that our conclusions are not largely due to a small fraction of poor predictions. Table 2 shows that all three performance metrics are consistent in their relative rankings of the various methods.

Table 3 shows the same results for LOFO cross-validation. The prediction errors for the spatial mean remain the same, but the rest of the errors are larger than with LOOO cross-validation, reflecting the more challenging nature of the LOFO prediction task. Even in this case, there are still distinct advantages to be gained by appropriate modeling of the anomalies.

Table 3: Same as Table 2 but for leave-one-float-out (LOFO) cross-validation.

Pressure level	Perf. metric	Spatial mean	Reference model	Space (1 month)	Space (3 months)	Space-time (3 months)
10 db	RMSE	0.8889	0.7177	0.6823 (4.9 %)	0.6954 (3.1 %)	0.6489 (9.6 %)
	Q ₃ AE	0.8670	0.6107	0.5776 (5.4 %)	0.5987 (2.0 %)	0.5222 (14.5 %)
	MdAE	0.4750	0.3165	0.2981 (5.8 %)	0.3062 (3.2 %)	0.2552 (19.3 %)
300 db	RMSE	0.8149	0.7686	0.7486 (2.6 %)	0.7483 (2.6 %)	0.7388 (3.9 %)
	Q ₃ AE	0.6320	0.5942	0.5733 (3.5 %)	0.5666 (4.6 %)	0.5556 (6.5 %)
	MdAE	0.3062	0.2856	0.2753 (3.6 %)	0.2732 (4.3 %)	0.2664 (6.7 %)
1500 db	RMSE	0.1337	0.1373	0.1308 (4.8 %)	0.1313 (4.4 %)	0.1307 (4.8 %)
	Q ₃ AE	0.1043	0.1015	0.0976 (3.9 %)	0.0973 (4.2 %)	0.0959 (5.6 %)
	MdAE	0.0530	0.0511	0.0499 (2.3 %)	0.0491 (3.7 %)	0.0484 (5.3 %)

The ranking of the models and the general conclusions are otherwise the same as above, expect for two differences: First, here the 3-month spatial model (model 4) does not significantly improve upon the 1-month model (model 2) and can in fact even perform worse. This happens because the model confuses spatial and temporal variation and highlights the importance of using a spatio-temporal covariance model. Second, at 1500 db, the RMSE of the reference model is slightly larger than the RMSE of the spatial mean. As discussed above, this may happen because of a few values in the right tail of the squared prediction error distribution, but may also indicate that the Roemmich–Gilson covariance parameters are not well-suited for this depth. In comparison, all the data-driven models perform better than the spatial mean, as expected.

The cross-validation results for the Student nugget are given in the supplement [36]. The Student models tend to perform worse than the comparable Gaussian models. This happens because they smooth out non-Gaussian high frequency features (eddies in particular) by including them in the nugget term. Nevertheless, the same conclusion that the spatio-temporal model outperforms the purely spatial model remains true. Even though the Student models have inferior point prediction performance, they offer significant advantages in uncertainty quantification (see Section 4(c)).

To summarize, these results highlight the importance of including time in the mapping and allowing the covariance parameters to change with location and depth. Indeed, the largest improvements are observed at 10 db, where one would intuitively expect the data-driven covariances to differ the most from the Roemmich–Gilson model (see Section 2(b)). To put these results into context, it is important to keep in mind that statistical procedures typically converge at sublinear rates as the amount of data increases. For example, assuming a $1/\sqrt{n}$ rate of convergence, a 20 % improvement in the predictive performance translates into 56 % more data. This would correspond to deploying roughly 2,000 additional floats at a cost of 30 million USD (one Argo float costs approximately 15,000 USD [38]). Similarly, even a 10 % performance improvement would correspond to approximately 23 % more data at a cost of some 12 million USD. These costs are even higher if one takes into account the need to replenish the array and the cost of data handling.

(c) Uncertainty quantification

We next investigate the uncertainty quantification performance of the different models. Figure 5 shows $\text{Var}(y_i^*|\mathbf{y}_i, \hat{\boldsymbol{\theta}}, \hat{\sigma}^2)/(\hat{\phi} + \hat{\sigma}^2)$, i.e., the ratio of the post-data and pre-data variances, for the locally stationary 3-month spatio-temporal model with a Gaussian nugget (model 5) at 10 db, 300 db and 1500 db in February 2012. Also shown is the same ratio for the reference model (model 1) at 10 db. Since the uncertainties of Gaussian process models depend only on the covariance parameters and the observation locations, the uncertainty of the reference model at 300 db and 1500 db (not shown) looks essentially the same the uncertainty at 10 db as the Roemmich–Gilson covariance model is the same at all depths (there are minor differences due to some profiles not extending all the way from 10 db to 1500 db). By contrast, the locally stationary uncertainties are vastly different at different depths. This happens because the estimated covariance parameters vary significantly as a function of depth (see Section 4(d)). Based on the anomalies shown in Figure 4, it makes intuitive sense that the uncertainties near the surface should be quite different from the uncertainties at greater depths. Note also that in the Roemmich–Gilson model with its fixed noise-to-signal variance ratio $\sigma^2/\phi = 0.15$, the post-data-to-pre-data variance ratio shown in Figure 5(d) does not depend on how the GP variance ϕ is chosen. By contrast, the rest of the results in this section require an estimate of ϕ (see Section 4(a)).

In order to study the uncertainty quantification performance in a more quantitative way, we cross-validate the entire predictive distribution for the different interpolation methods. With the Gaussian nugget, the cross-validated predictive distribution for $y_{i,j}$ is $(y_{i,j}|\mathbf{y}_{i\setminus(i,j)}, \hat{\boldsymbol{\theta}}, \hat{\sigma}^2) \sim N(\hat{m}_{-(i,j)}^G, \hat{v}_{-(i,j)}^G)$, where $\mathbf{y}_{i\setminus(i,j)}$ is \mathbf{y}_i with either $y_{i,j}$ removed (LOOO) or all observations with the same float ID as $y_{i,j}$ removed (LOFO). The predictive mean $\hat{m}_{-(i,j)}^G$ and variance $\hat{v}_{-(i,j)}^G$ are as in Equation (10), but with the appropriate data points removed. The covariance parameters $\hat{\boldsymbol{\theta}}$ and $\hat{\sigma}^2$ are taken from the MLEs at the grid point closest to $y_{i,j}$. Conditional on $(\mathbf{y}_{i\setminus(i,j)}, \hat{\boldsymbol{\theta}}, \hat{\sigma}^2)$, it then follows that $(y_{i,j} - \hat{m}_{-(i,j)}^G)/\sqrt{\hat{v}_{-(i,j)}^G} \sim N(0, 1)$ so we can compare the sample quantiles of $\{(y_{i,j} - \hat{m}_{-(i,j)}^G)/\sqrt{\hat{v}_{-(i,j)}^G}, i = 1, \dots, n, j = 1, \dots, m_i\}$ to the corresponding quantiles of the standard Gaussian distribution.

With the Student nugget, the cross-validated Laplace approximated predictive distribution is $(y_{i,j}|\mathbf{y}_{i\setminus(i,j)}, \hat{\boldsymbol{\theta}}, \hat{\sigma}^2, \hat{\nu}) \stackrel{a}{\sim} P_{Z_1+Z_2}$, where $P_{Z_1+Z_2}$ denotes the distribution of $Z_1 + Z_2$, with $Z_1 \sim N(\hat{m}_{-(i,j)}^S, \hat{v}_{-(i,j)}^S)$, where $\hat{m}_{-(i,j)}^S$ and $\hat{v}_{-(i,j)}^S$ are as in Equation (18), but with the appropriate data points removed when computing the Laplace approximation, $Z_2 \sim \hat{\sigma}t_{\hat{\nu}}$ and Z_1 and Z_2 are independent. Let F denote the cumulative distribution function of $P_{Z_1+Z_2}$. Then, conditional on $(\mathbf{y}_{i\setminus(i,j)}, \hat{\boldsymbol{\theta}}, \hat{\sigma}^2, \hat{\nu})$, we have that $F(y_{i,j}) \sim U(0, 1)$, where $U(0, 1)$ is the uniform distribution on $(0, 1)$. Letting Φ denote the standard Gaussian cumulative distribution function, it follows that $\Phi^{-1}(F(y_{i,j})) \sim N(0, 1)$ and we can again compare the sample quantiles of $\{\Phi^{-1}(F(y_{i,j})), i = 1, \dots, n, j = 1, \dots, m_i\}$ to the quantiles of the standard Gaussian distribution. Since F is not available in closed form, we compute its values by Monte Carlo sampling. The model parameters $(\hat{\boldsymbol{\theta}}, \hat{\sigma}^2, \hat{\nu})$ are taken to be the Laplace approximated MLEs at the grid point closest to $y_{i,j}$.

We compare the calibration of the reference model (model 1), the locally stationary 1-month spatial model with a Gaussian and a Student nugget (models 2 and 3) and the locally stationary 3-month spatio-temporal model with a Gaussian and a Student nugget (models 5 and 6). For each method, let q_{sample} denote the cross-validated sample quantile on the $N(0, 1)$ scale and q_{theory} the corresponding theoretical $N(0, 1)$ quantile. Figure 6 shows the quantile

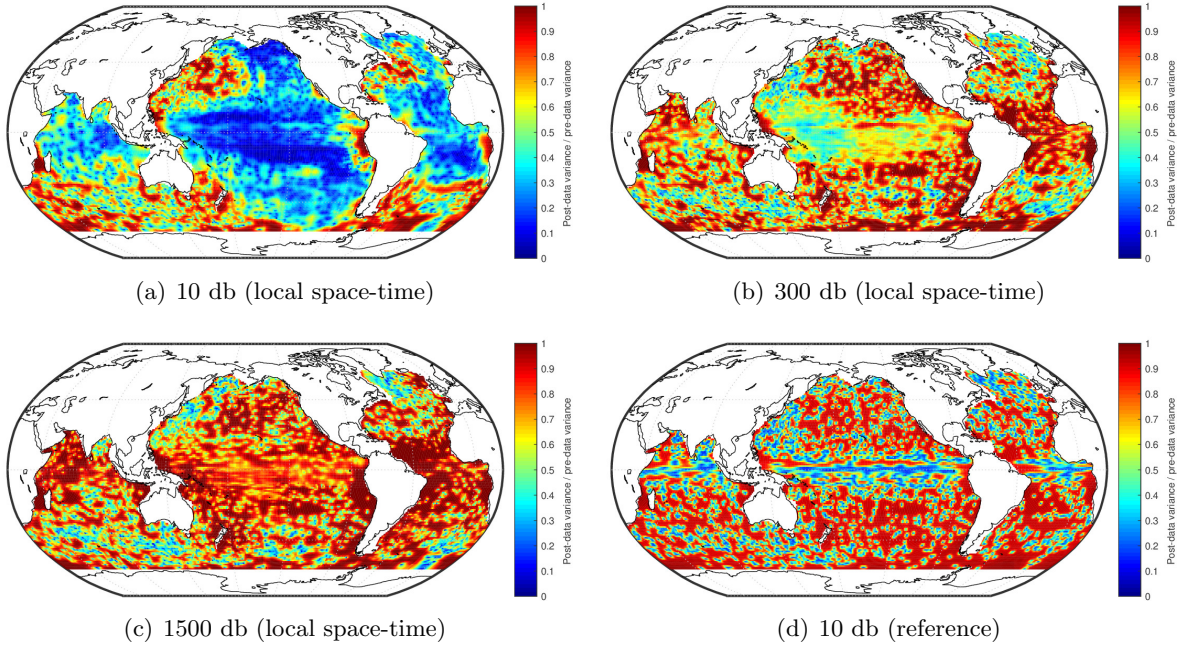


Figure 5: Post-data-to-pre-data variance ratio $\text{Var}(y_i^* | \mathbf{y}_i, \hat{\boldsymbol{\theta}}, \hat{\sigma}^2) / (\hat{\phi} + \hat{\sigma}^2)$ in February 2012 for the locally stationary 3-month spatio-temporal model with a Gaussian nugget (model 5) at 10 db, 300 db and 1500 db (Figures (a)–(c)) and for the Roemmich–Gilson-like reference model (model 1) at 10 db (Figure (d)). Because the Roemmich–Gilson covariance is the same at all depths, the variance ratios at 300 db and 1500 db (not shown) are essentially the same as the one shown at 10 db, while the locally stationary models produce uncertainties that vary as expected with depth.

difference $q_{\text{sample}} - q_{\text{theory}}$ plotted against the theoretical quantile q_{theory} at 300 db for LOOO cross-validation. This can be understood as the usual QQ plot with the identity line subtracted—plotting the quantiles this way helps visualize differences at the core of the distribution. The reference model is poorly calibrated with both tails of the data distribution much wider than those of the predictive distribution. The locally stationary models with the Gaussian nugget improve the calibration, but the data distribution still has heavier tails and a pointier core than the predictive distribution. We understand this as evidence of non-Gaussian heavy tails in Argo temperature data. The Student nugget provides a way to account for these heavy tails and indeed the calibration of the Student models is much better than that of the fully Gaussian models. Even though some miscalibration still remains, the overall improvement of the locally stationary Student models over the reference model is quite substantial. We also note that the spatial and spatio-temporal models are essentially equally well-calibrated in the present setting.

The quantile plots in Figure 6 translate directly into the coverage probability of the predictive intervals. Table 4 shows the LOOO cross-validated empirical coverages and interval lengths for 68 %, 95 % and 99 % predictive intervals at 300 db for the same models as in Figure 6. As expected based on Figure 6, the reference model undercovers at all confidence levels. The locally stationary models overcover at 68 % level, are well-calibrated at 95 % level and undercover at 99 % level. At 68 % and 99 % levels, the coverage of the Student intervals is much closer to the nominal level than the coverage of the Gaussian intervals. The space-time intervals are always shorter than the corresponding spatial intervals, which is consistent with the performance improvements observed in Section 4(b).

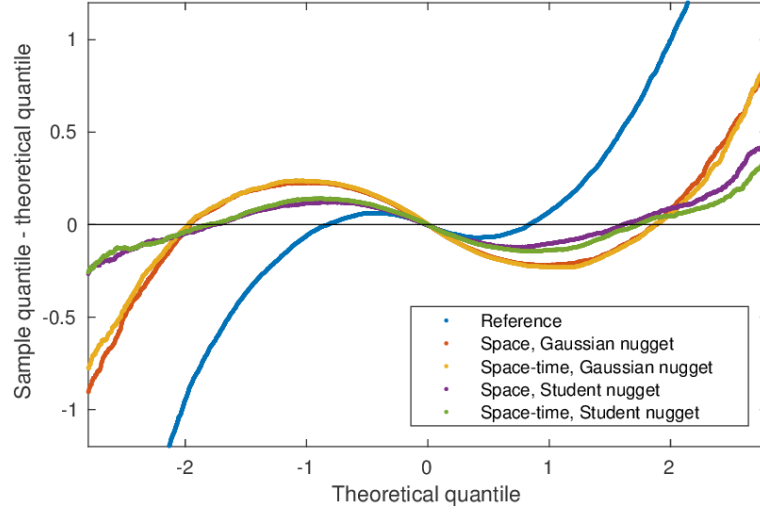


Figure 6: The difference of the cross-validated sample quantile and the corresponding standard Gaussian theoretical quantile ($q_{\text{sample}} - q_{\text{theory}}$) plotted against the theoretical quantile (q_{theory}) for leave-one-observation-out (LOOO) cross-validation at 300 db. The compared models are the Roemmich–Gilson-like reference model (model 1), the locally stationary 1-month spatial and 3-month spatio-temporal models with a Gaussian nugget (models 2 and 5) and the corresponding models with a Student nugget (models 3 and 6). The closer the curves are to a horizontal straight line at 0, the better the calibration of the predictive distributions.

Table 4: Empirical coverage and length (in °C) of the predictive intervals at 300 db for leave-one-observation-out (LOOO) cross-validation. The models are the same as in Figure 6.

Confidence level	Method	Empirical coverage	Mean length	Median length
68 %	Reference	0.6607	0.7511	0.6435
	Space, Gaussian nugget	0.7745	0.9749	0.8728
	Space-time, Gaussian nugget	0.7800	0.8722	0.7816
	Space, Student nugget	0.7261	0.8427	0.7621
	Space-time, Student nugget	0.7389	0.7697	0.7049
95 %	Reference	0.8755	1.4721	1.2612
	Space, Gaussian nugget	0.9482	1.9108	1.7107
	Space-time, Gaussian nugget	0.9490	1.7095	1.5320
	Space, Student nugget	0.9432	1.9918	1.7525
	Space-time, Student nugget	0.9452	1.8543	1.6192
99 %	Reference	0.9329	1.9347	1.6575
	Space, Gaussian nugget	0.9777	2.5112	2.2483
	Space-time, Gaussian nugget	0.9793	2.2466	2.0134
	Space, Student nugget	0.9835	3.9385	2.6417
	Space-time, Student nugget	0.9844	3.8086	2.3976

The quantile plots, empirical coverages and interval lengths for the other depths and for LOFO cross-validation are given in the supplement [36]. The LOOO conclusions at 10 db are otherwise similar to 300 db, except that the spatio-temporal models appear to have worse calibration than the spatial models. This might be an indication that the spatio-temporal dependence structure near the surface is more complicated than what our exponential covariance function with geometric anisotropy can capture. For LOOO at 1500 db, the spatial and spatio-temporal models are equally well-calibrated, but there also appears to be less non-Gaussianity and the Student nugget provides only limited improvement over the Gaussian nugget. The basic conclusions that locally stationary modeling improves the calibration over the reference model and that the Student nugget improves over the Gaussian nugget still largely hold true for LOFO cross-validation, but here the spatio-temporal models are slightly worse calibrated than the spatial models at all depths. The spatio-temporal models nonetheless provide distinct advantages in terms of the length of the intervals. In these cases, the optimal choice of intervals depends on the relative importance given to accurate calibration and short interval length.

(d) Local estimates of dependence structure

In this section, we investigate the locally estimated model parameters and demonstrate that they exhibit physically meaningful structure. We study in detail the fitted 3-month spatio-temporal model with a Gaussian nugget (model 5). Analogous plots for the other models are given in the supplement [36].

Figure 7 shows the estimated total variance $\hat{\phi} + \hat{\sigma}^2$ at 10 db, 300 db and 1500 db. At 10 db and 300 db, we can clearly see the large variability in the western sides of the ocean basins caused by the strong western boundary currents. For example, the Kuroshio Current off the coast of Japan, the Gulf Stream in the North-West Atlantic, the Brazil Current in the South-West Atlantic and the Agulhas retroflexion and leakage areas around the southern tip of Africa (see Section 11.4.2 in [27]) can be easily identified at both depths. The East Australian Current is also visible at 300 db. By contrast, the eastern sides of the ocean basins have significantly less variability, as expected. A notable exception is North-Eastern Atlantic at 1500 db which has much more variability than other regions at this depth. We suspect that this variability can be attributed to eddies caused by outflow from the Mediterranean Sea [39]. The bands of high variability at roughly 10°N and 10°S at 10 db in the Pacific Ocean are likely to be related to Rossby waves at those latitudes.

We next study the estimated ranges of zonal, meridional and temporal dependence in Argo temperature data. We do this by plotting maps of the correlation implied by the locally estimated covariance parameters at given zonal, meridional and temporal lags. We plot the maps in the correlation space instead of the range parameter space since there is some degree of ambiguity with regards to what fraction of the variability is attributed to the nugget effect in the MLE fits (at intermediate lags, a large nugget variance σ^2 , a small GP variance ϕ and a large range parameter θ_{lat} , θ_{lon} or θ_t can imply almost the same fitted correlation as a small nugget σ^2 , a large GP variance ϕ and a small range parameter θ_{lat} , θ_{lon} or θ_t).

Figure 8 shows the fitted correlation at the zonal lag $\Delta x_{\text{lon}} = 800$ km (with $\Delta x_{\text{lat}} = 0$, $\Delta t = 0$ and taking the conversion latitude into account when converting degrees into kilometers). The range of the zonal dependence varies considerably as a function of depth, with much longer ranges near the surface than at greater depths. The long-range dependence near the surface is likely to be caused by interaction with the atmosphere. There is also a general tendency to have zonally elongated ranges in the Equatorial regions. The estimated ranges are generally longer in the Pacific Ocean than in the Indian or Atlantic Oceans. At 10 db in the Pacific Ocean, there

is again evidence of patterns related to Equatorial Rossby and Kelvin waves.

Figure 9 shows the fitted correlation at the meridional lag $\Delta x_{\text{lat}} = 800$ km (with $\Delta x_{\text{lon}} = 0$, $\Delta t = 0$). The general conclusions are similar to Figure 8: the ranges are longer close to the surface and in the Equatorial regions. The distinct patch of long-range dependence in the Equatorial West Pacific is likely to be related to the Pacific thermocline which is tilted westward along the Equator. The meridional ranges also show interesting patterns in areas where the Amazon River and the Congo River flow into the Atlantic Ocean. Note that all the plots in Figures 8 and 9 are on the same (logarithmic) color scale and can thus be compared directly. This comparison shows that the dependence structure is clearly anisotropic with the zonal ranges longer than the meridional ones.

Figure 10 shows the fitted correlation at the temporal lag $\Delta t = 10$ days (with $\Delta x_{\text{lat}} = 0$ and $\Delta x_{\text{lon}} = 0$). There are differences in the correlation patterns between the three depths, but interestingly the overall magnitude of the temporal correlation changes relatively little with depth. There does seem to be a slight tendency for the temporal correlation to increase with depth in the Southern Ocean and to decrease with depth in most other areas, but these changes are much less pronounced than in the case of the zonal and meridional ranges (Figures 8 and 9).

Ninove et al. [40] have previously estimated dependence scales using Argo data. They estimate the range parameters (which are often called “decorrelation scales” by oceanographers) by dividing the global ocean into large disjoint boxes and then use a weighted least-squares variogram fit to data within each box. They only consider spatial dependence and do not provide estimates of temporal ranges. In comparison, our moving-window approach includes the temporal dimension and provides information about the dependence structure at much finer horizontal resolution. It is also well-established in the spatial statistics literature that MLE fits should be preferred over variogram fits [18]. Nevertheless, many of our conclusions qualitatively agree with those of Ninove et al. They also find longer ranges near the surface, elongation in the tropics, zonal anisotropy and shorter ranges in the Indian and Atlantic Oceans. However, we do not find evidence for the strong increase in spatial ranges below 700 m that Ninove et al. observe. Instead, our spatial ranges are almost always shorter at 1500 db than at 300 db. We suspect that the effect seen by Ninove et al. is an artifact caused by the pre-Argo mean field they use. This mean field is likely to be poorly constrained at depth, where little data was available before Argo, and any residual mean effect would show up as increased spatial dependence in the empirical variograms.

5 Conclusions and outlook

We have demonstrated that the spatio-temporal dependence structure of ocean temperatures can be estimated from Argo data using local moving-window maximum likelihood estimates. The resulting fully data-driven nonstationary anomaly fields and their uncertainties yield substantial improvements over existing state-of-the-art methods. The improvements in point prediction accuracy are comparable to deploying hundreds of new Argo floats. There is also evidence of non-Gaussian heavy tails in Argo temperature data and taking this into account is crucial for obtaining well-calibrated uncertainties. The estimated covariance models exhibit physically sensible patterns that can be analyzed further to test theories of large-scale ocean circulation.

Statistically, this work demonstrates how well-suited moving-window Gaussian process regression is for handling modern massive nonstationary spatio-temporal data sets. This approach helps address in a straightforward manner challenges related to both nonstationarity and computational complexity, issues that affect analysis of almost any large-scale environmental data

set. In the present work, we developed a version of the moving-window approach that uses a Student- t distributed nugget effect to address heavy tails in Argo data. To the best of our knowledge, Student nugget has not been previously used in conjunction with moving-window Gaussian process regression. While spatial and spatio-temporal moving-window techniques have been around since the seminar work of Haas [11, 12], we feel that there is much room for further application and methodological development on this front.

To produce our interpolated temperature anomalies, we used the fairly simple exponential covariance function with geometric anisotropy along the zonal, meridional and temporal axes (see Equation (6)). We have compared the model fit to empirical covariances in various regions and generally find the two to be in reasonably good agreement. We have also investigated more complex space-time covariance models including the Matérn model [18], the Gneiting model [41] and geometric anisotropy that is not constrained to be aligned with the latitude-longitude coordinate axes. We have experimented with these models in selected regions of the Pacific Ocean at 300 db. In each case, we found only minor improvements in the likelihood values and point predictions in comparison to the simple exponential covariance function. At the same time, the estimated covariance parameters became very challenging to interpret and validate (since several combinations of the model parameters can represent almost the same covariance structure) and the likelihood computations were much too slow to be practical on a global scale. These extensions could still be useful at other depths or regions, but the interpretability and computations remain problematic. Another potentially useful extension, which we have not yet explored, is to add a velocity term in the spatio-temporal covariance, as is for example done in mapping of satellite altimetry data [42].

While the Student prediction intervals clearly yield improved uncertainty quantification, the present implementation of the Student nugget suffers from algorithmic instabilities. This can be easily seen in the fitted model parameters shown in the supplementary material [36]. These instabilities are likely to be related to the nonconcave optimization problem that needs to be solved as part of the Laplace approximation [32]. Alternatively, it might be that the Laplace approximation itself is not appropriate in some parts of the ocean. We experimented with an alternative implementation of the Laplace approximation [43] but observed similar instabilities. Further research is needed to understand the precise cause of these instabilities before the Student fits can be recommended for use in an actual data product.

This work has only scratched the surface in terms of the statistical research that can be done with the Argo data set. We sketch below some potential extensions and directions for future work:

- In this work, we have focused on Argo temperature data only. In principle, similar locally stationary interpolation is also applicable to salinity data, but the challenge is that especially at larger depths the variability of the salinity field is so small that instrumental errors can no longer be ignored. This means that more careful modeling of the nugget effect to include measurement error is needed. We also feel that when mapping both temperature and salinity, one should take into account their correlation which requires modeling the spatio-temporal cross-covariance between the two fields. This cross-covariance function can in fact be of scientific interest in its own right.
- Maps of the locally estimated covariance models (see Figures 7–10) tend to sometimes have zonal or meridional stripes that are related to the sharp boundary of the $20^\circ \times 20^\circ$ moving window. These stripes could be removed by replacing the moving window by a smooth kernel function as in [44]. Since it is often possible to represent almost the same covariance

structure by various combinations of the model parameters, we also sometimes see abrupt transitions from one parameter configuration to another. It should be possible to fix this issue by finding a way to borrow strength across the nearby grid points in the parameter estimates. One could, for instance, envision using a Bayesian hierarchical model, where the maps of the local model parameters are themselves modeled as spatially dependent stochastic processes, as in [45], for example. However, it seems challenging to find a way to carry out the computations at the scale of the global ocean under such model.

- The only type of non-Gaussianity we considered in this work is spatially and temporally uncorrelated Student- t distributed heavy tails. However, further exploratory analysis of the mean-subtracted residuals reveals also the presence of skewness (especially near the surface) and regions where the distribution of the anomalies appears to be multimodal. It is also likely that the heavy-tailed features, which at least partially correspond to eddies, are spatially and temporally correlated (this would also help explain why the point prediction performance of the Student nugget models is inferior to the performance of the Gaussian nugget models). It would hence be interesting to consider space-time models with more versatile non-Gaussian structure. Stochastic partial differential equations, as in [46], may provide a way to construct such models.
- In the present work, we have not exploited dependence across depth levels. A natural extension would be to carry out full 4D mapping by including the vertical dimension in the covariance structure. In principle, the moving-window approach can easily be extended to this situation by considering observations at nearby depths. However, modeling the vertical covariance structure seems nontrivial since the vertical direction contains phenomena that are fundamentally different from the other dimensions. For example, ocean stratification can cause abrupt vertical changes, while eddies exhibit coherent vertical structure. One would ideally also like to find a way to incorporate the constraint that density must be a monotonically increasing function of depth.
- In this work, we have only considered point-wise uncertainties. However, many scientifically important quantities are functionals of the temperature and salinity fields (or some field derived from these two quantities). For example, the ocean heat content is essentially an integral of the temperature field. To provide uncertainties for functionals requires access to covariances or conditional simulations. Neither of these quantities can be directly obtained from the moving-window approach considered here. It should, however, be possible to combine the local covariance models into a valid global nonstationary model using the approach developed in [45]. This global model could then be used to compute the predictive covariance matrix or to produce conditional simulations, although it is not immediately clear if all the necessary computations are feasible on the scale of the Argo data set.

Access to data, code and supplementary material

The results presented in this paper are based on the May 8, 2017 snapshot of the Argo GDAC (<http://doi.org/10.17882/42182#50059>). The Matlab code is available at <https://github.com/mkuusela/ArgoMappingPaper> and supplementary material can be found at <https://github.com/mkuusela/ArgoMappingPaper/raw/master/Doc/supplement.pdf>.

Acknowledgments

We are grateful to Fred Bingham, Chen Chen, Bruce Cornuelle, Donata Giglio, John Gilson, Sarah Gille, Alison Gray, Malte Jansen, Alice Marzocchi, Matt Mazloff, Breck Owens, Dean Roemmich, Megan Scanderbeg and Nathalie Zilberman for many discussions about Argo data, oceanography and previous mapping algorithms as well as for helpful feedback on preliminary results throughout this project.

Most of this work was carried out while MK was at the University of Chicago, Department of Statistics. This work was supported by the STATMOS Research Network (NSF awards 1106862, 1106974 and 1107046), the US Department of Energy grant no. DE-SC0002557 and the National Science Foundation Grant DMS-1638521 to the Statistical and Applied Mathematical Sciences Institute. This work was completed in part using computational resources provided by the University of Chicago Research Computing Center.

Argo data were collected and made freely available by the International Argo Program and the national programs that contribute to it (<http://www.argo.ucsd.edu>, <http://argo.jcommops.org>). The Argo Program is part of the Global Ocean Observing System.

Disclaimer

Any opinions, findings and conclusions or recommendations expressed in this material are those of the authors and do not necessarily reflect the views of the National Science Foundation or the US Department of Energy.

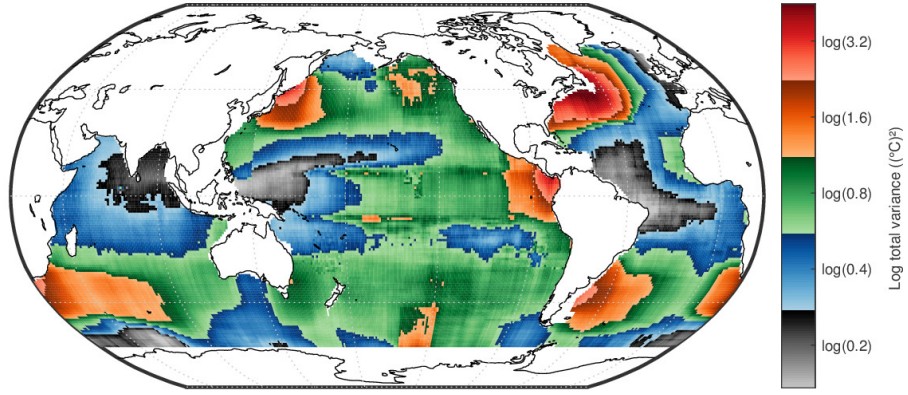
References

- [1] Dean Roemmich, John Church, John Gilson, Didier Monselesan, Philip Sutton, and Susan Wijffels. Unabated planetary warming and its ocean structure since 2006. *Nature Climate Change*, 5:240–245, 2015.
- [2] Alison R. Gray and Stephen C. Riser. A global analysis of Sverdrup balance using absolute geostrophic velocities from Argo. *Journal of Physical Oceanography*, 44(4):1213–1229, 2014.
- [3] Zhengguang Zhang, Wei Wang, and Bo Qiu. Oceanic mass transport by mesoscale eddies. *Science*, 345(6194):322–324, 2014.
- [4] Tyler D. Hennon, Stephen C. Riser, and Matthew H. Alford. Observations of internal gravity waves by Argo floats. *Journal of Physical Oceanography*, 44(9):2370–2386, 2014.
- [5] L. Cheng, J. Zhu, and R. L. Srivier. Global representation of tropical cyclone-induced short-term ocean thermal changes using Argo data. *Ocean Science*, 11(5):719–741, 2015.
- [6] You-Soon Chang, Shaoqing Zhang, Anthony Rosati, Thomas L. Delworth, and William F. Stern. An assessment of oceanic variability for 1960–2010 from the GFDL ensemble coupled data assimilation. *Climate Dynamics*, 40:775–803, 2013.
- [7] Dean Roemmich and John Gilson. The 2004–2008 mean and annual cycle of temperature, salinity, and steric height in the global ocean from the Argo Program. *Progress in Oceanography*, 82:81–100, 2009.

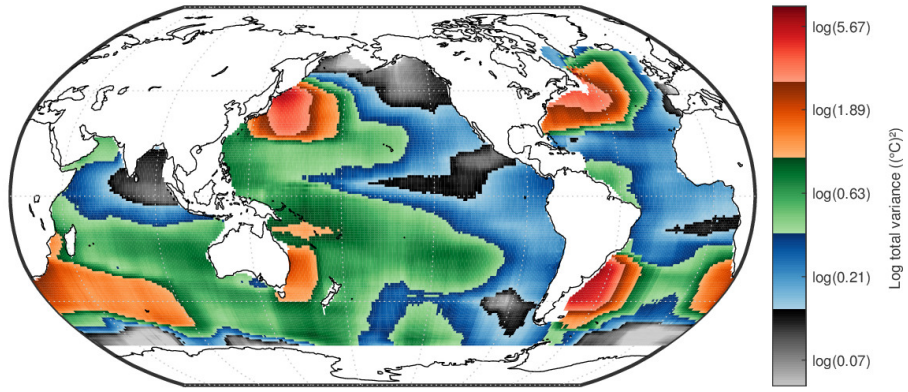
- [8] Sunke Schmidtke, Gregory C. Johnson, and John M. Lyman. MIMOC: A global monthly isopycnal upper-ocean climatology with mixed layers. *Journal of Geophysical Research: Oceans*, 118(4):1658–1672, 2013.
- [9] Simon A. Good, Matthew J. Martin, and Nick A. Rayner. EN4: Quality controlled ocean temperature and salinity profiles and monthly objective analyses with uncertainty estimates. *Journal of Geophysical Research: Oceans*, 118(12):6704–6716, 2013.
- [10] Noel Cressie and Christopher K. Wikle. *Statistics for Spatio-Temporal Data*. John Wiley & Sons, 2011.
- [11] Timothy C. Haas. Lognormal and moving window methods of estimating acid deposition. *Journal of the American Statistical Association*, 85(412):950–963, 1990.
- [12] Timothy C. Haas. Local prediction of a spatio-temporal process with an application to wet sulfate deposition. *Journal of the American Statistical Association*, 90(432):1189–1199, 1995.
- [13] Dorit M. Hammerling, Anna M. Michalak, and S. Randolph Kawa. Mapping of CO₂ at high spatiotemporal resolution using satellite observations: Global distributions from OCO-2. *Journal of Geophysical Research: Atmospheres*, 117:D06306, 2012.
- [14] Dorit M. Hammerling, Anna M. Michalak, Christopher O’Dell, and S. Randolph Kawa. Global CO₂ distributions over land from the Greenhouse Gases Observing Satellite (GOSAT). *Geophysical Research Letters*, 39:L08804, 2012.
- [15] J. M. Tadić, X. Qiu, V. Yadav, and A. M. Michalak. Mapping of satellite Earth observations using moving window block kriging. *Geoscientific Model Development*, 8(10):3311–3319, 2015.
- [16] Jovan M. Tadić, Xuemei Qiu, Scot Miller, and Anna M. Michalak. Spatio-temporal approach to moving window block kriging of satellite data v1.0. *Geoscientific Model Development*, 10(2):709–720, 2017.
- [17] Noel A. C. Cressie. *Statistics for Spatial Data*. John Wiley & Sons, revised edition, 1993.
- [18] Michael L. Stein. *Interpolation of Spatial Data: Some Theory for Kriging*. Springer, 1999.
- [19] Roger Daley. *Atmospheric Data Analysis*. Cambridge University Press, 1991.
- [20] Francis P. Bretherton, Russ E. Davis, and C. B. Fandry. A technique for objective analysis and design of oceanographic experiments applied to MODE-73. *Deep Sea Research*, 23(7):559–582, 1976.
- [21] Carl Edward Rasmussen and Christopher K. I. Williams. *Gaussian Processes for Machine Learning*. MIT Press, 2006.
- [22] Alison R. Gray and Stephen C. Riser. A method for multiscale optimal analysis with application to Argo data. *Journal of Geophysical Research: Oceans*, 120(6):4340–4356, 2015.
- [23] Dean Roemmich et al. On the design and implementation of Argo: A global array of profiling floats. International CLIVAR Project Office Report 21, 1998. Available online at <http://www.argo.ucsd.edu/argo-design.pdf>.

- [24] Stephen C. Riser et al. Fifteen years of ocean observations with the global Argo array. *Nature Climate Change*, 6:145–153, 2016.
- [25] Annie Wong, Robert Keeley, Thierry Carval, and the Argo Data Management Team. Argo quality control manual for CTD and trajectory data, 2015. <http://dx.doi.org/10.13155/33951>.
- [26] Dean Roemmich and John Gilson. Roemmich–Gilson Argo climatology website, retrieved December 1, 2016. http://sio-argo.ucsd.edu/RG_Climatology.html.
- [27] Lynne D. Talley, George L. Pickard, William J. Emery, and James H. Swift. *Descriptive Physical Oceanography: An Introduction*. Elsevier, 6th edition, 2011.
- [28] Florent Gasparin, Dean Roemmich, John Gilson, and Bruce Cornuelle. Assessment of the upper-ocean observing system in the Equatorial Pacific: The role of Argo in resolving intraseasonal to interannual variability. *Journal of Atmospheric and Oceanic Technology*, 32(9):1668–1688, 2015.
- [29] Fabienne Gaillard. ISAS-Tool Version 6: Method and configuration. Technical Report LPO-12-02, Ifremer, 2012.
- [30] Shigeki Hosoda, Tsuyoshi Ohira, and Tomoaki Nakamura. A monthly mean dataset of global oceanic temperature and salinity derived from Argo float observations. *JAMSTEC Report of Research and Development*, 8:47–59, 2008.
- [31] Mathworks. *Optimization Toolbox User’s Guide*, 2016. Release 2016a.
- [32] Jarno Vanhatalo, Pasi Jylänki, and Aki Vehtari. Gaussian process regression with Student- t likelihood. In Y. Bengio, D. Schuurmans, J. D. Lafferty, C. K. I. Williams, and A. Culotta, editors, *Advances in Neural Information Processing Systems 22*, pages 1910–1918. 2009.
- [33] Carl Edward Rasmussen and Hannes Nickisch. Gaussian Processes for Machine Learning (GPML) toolbox. *Journal of Machine Learning Research*, 11(Nov):3011–3015, 2010.
- [34] Carl E. Rasmussen and Hannes Nickisch. GPML Matlab code, version 4.0, October 19, 2016. Available at <http://www.gaussianprocess.org/gpml/code/matlab>.
- [35] Argo Program. Argo float data and metadata from Global Data Assembly Centre (Argo GDAC) – Snapshot of Argo GDAC of May 8th, 2017. SEANOE, 2017. <http://doi.org/10.17882/42182#50059>.
- [36] Mikael Kuusela and Michael L. Stein. Supplement to “Locally stationary spatio-temporal interpolation of Argo profiling float data”, 2017. Available at <https://github.com/mkuusela/ArgoMappingPaper/raw/master/Doc/supplement.pdf>.
- [37] Mikael Kuusela and Michael L. Stein. Matlab code for “Locally stationary spatio-temporal interpolation of Argo profiling float data”, 2017. Available at <https://github.com/mkuusela/ArgoMappingPaper>.
- [38] Argo Program. Frequently asked questions, retrieved October 22, 2017. <http://www.argo.ucsd.edu/FAQ.html>.

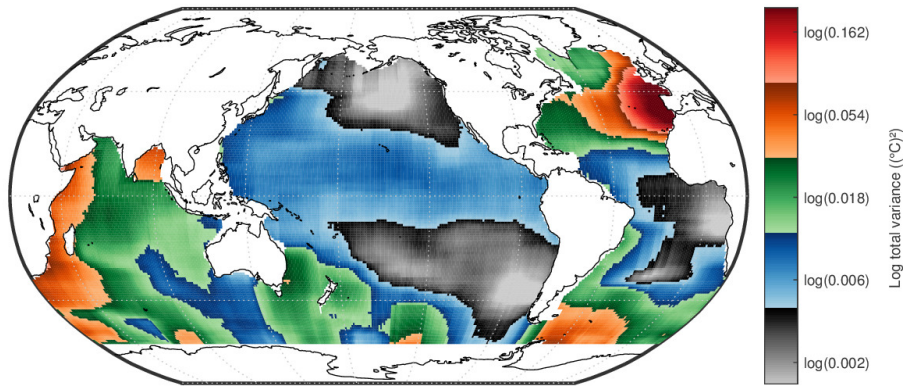
- [39] Michaela C. Iorga and M. Susan Lozier. Signatures of the Mediterranean outflow from a North Atlantic climatology: 1. Salinity and density fields. *Journal of Geophysical Research: Oceans*, 104(C11):25985–26009, 1999.
- [40] F. Ninove, P.-Y. Le Traon, E. Remy, and S. Guinehut. Spatial scales of temperature and salinity variability estimated from Argo observations. *Ocean Science*, 12(1):1–7, 2016.
- [41] Tilmann Gneiting. Nonseparable, stationary covariance functions for space-time data. *Journal of the American Statistical Association*, 97(458):590–600, 2002.
- [42] Marie-Isabelle Pujol, Yannice Faugère, Guillaume Taburet, Stéphanie Dupuy, Camille Pelloquin, Michael Ablain, and Nicolas Picot. DUACS DT2014: The new multi-mission altimeter data set reprocessed over 20 years. *Ocean Science*, 12(5):1067–1090, 2016.
- [43] Jarno Vanhatalo, Jaakko Riihimäki, Jouni Hartikainen, Pasi Jylänki, Ville Tolvanen, and Aki Vehtari. GPstuff: Bayesian modeling with Gaussian processes. *Journal of Machine Learning Research*, 14(Apr):1175–1179, 2013.
- [44] Ethan B. Anderes and Michael L. Stein. Local likelihood estimation for nonstationary random fields. *Journal of Multivariate Analysis*, 102:506–520, 2011.
- [45] Christopher J. Paciorek and Mark J. Schervish. Spatial modelling using a new class of nonstationary covariance functions. *Environmetrics*, 17(5):483–506, 2006.
- [46] Jonas Wallin and David Bolin. Geostatistical modelling using non-Gaussian Matérn fields. *Scandinavian Journal of Statistics*, 42(3):872–890, 2015.



(a) 10 db

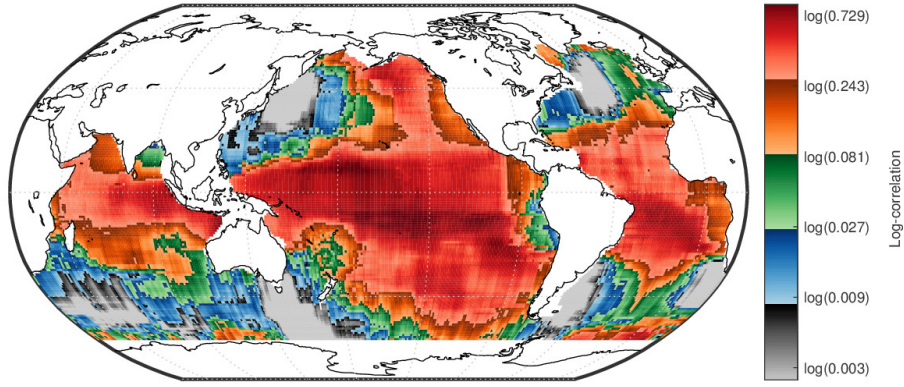


(b) 300 db

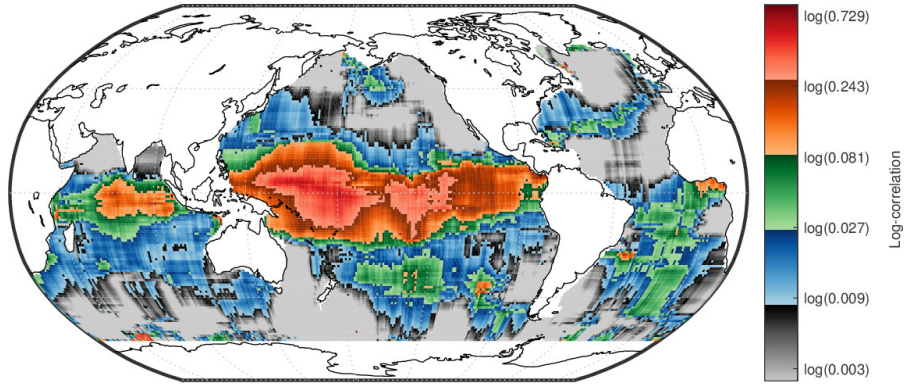


(c) 1500 db

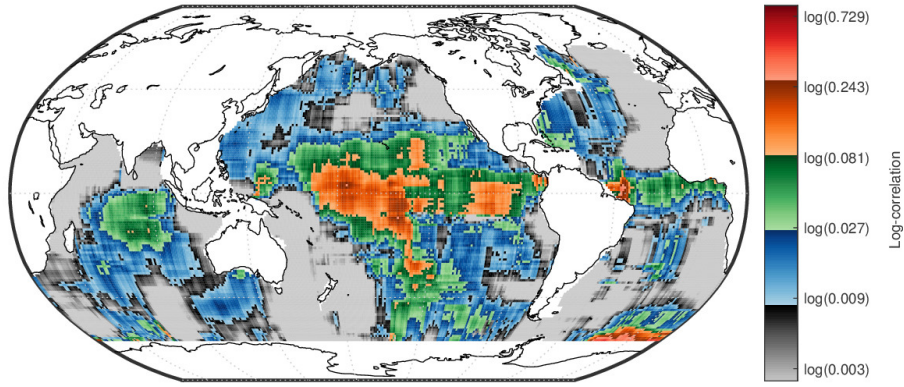
Figure 7: Estimated total variance $\hat{\phi} + \hat{\sigma}^2$ for the locally stationary 3-month spatio-temporal model with a Gaussian nugget (model 5).



(a) 10 db

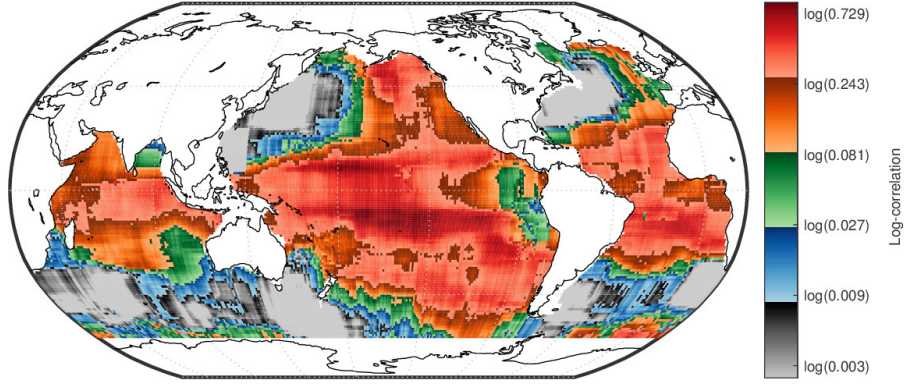


(b) 300 db

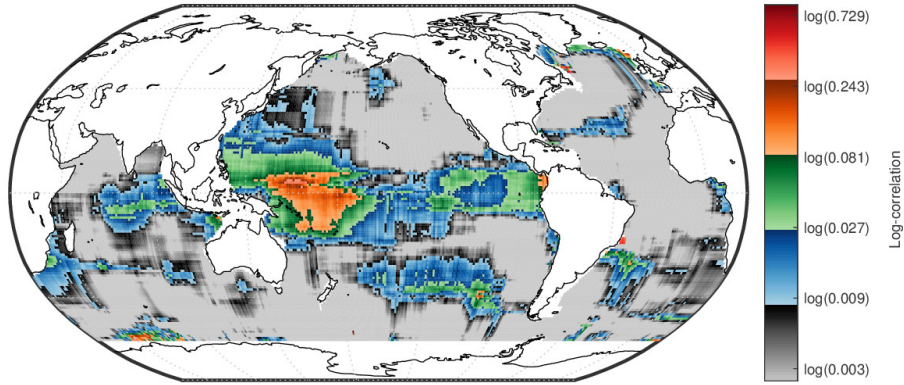


(c) 1500 db

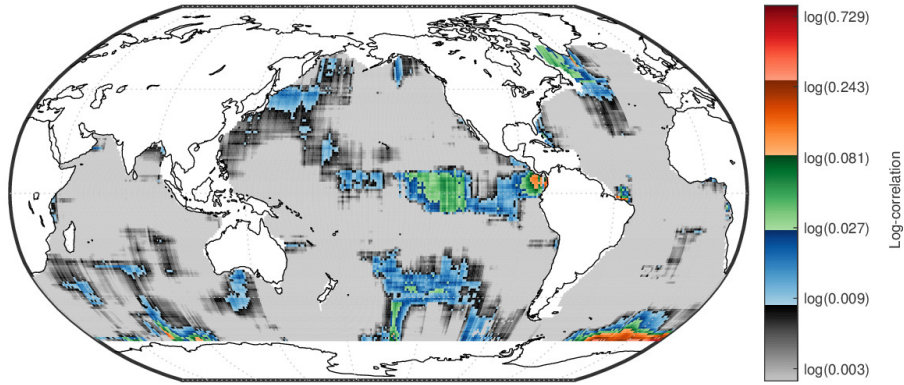
Figure 8: Fitted correlation at zonal lag $\Delta x_{\text{lon}} = 800$ km for the locally stationary 3-month spatio-temporal model with a Gaussian nugget (model 5). To facilitate comparison, all the panels here and in Figure 9 have the same color scales.



(a) 10 db

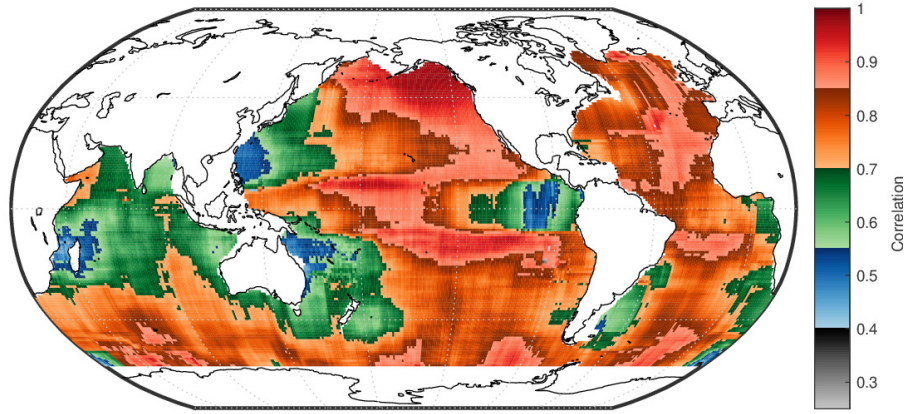


(b) 300 db

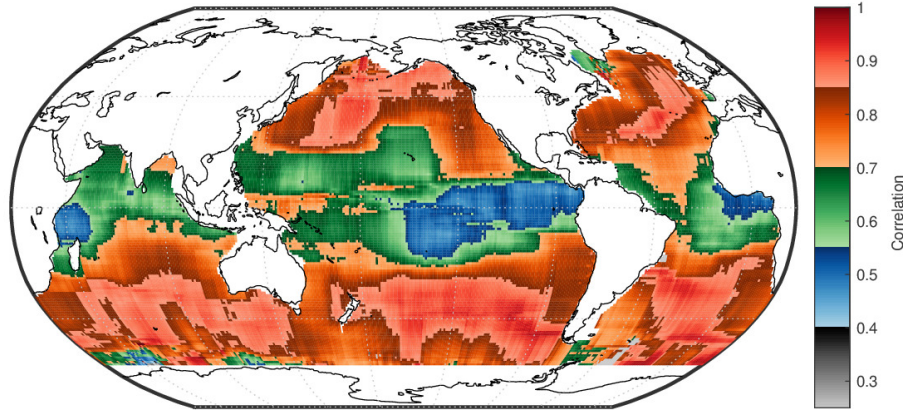


(c) 1500 db

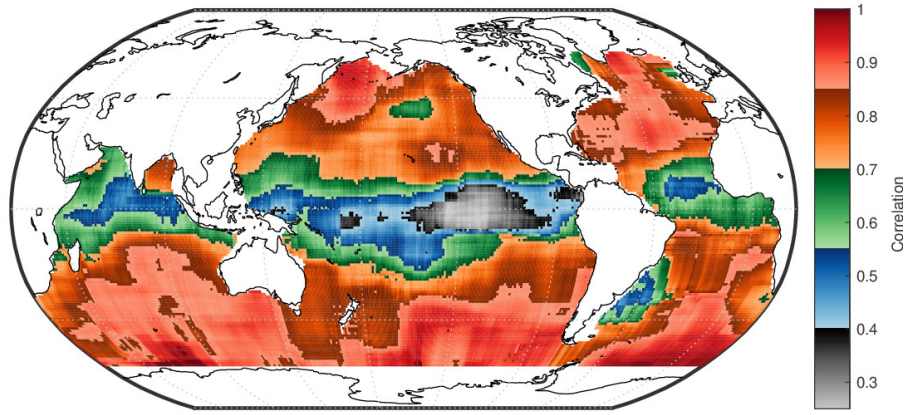
Figure 9: Fitted correlation at meridional lag $\Delta x_{\text{lat}} = 800$ km for the locally stationary 3-month spatio-temporal model with a Gaussian nugget (model 5). To facilitate comparison, all the panels here and in Figure 8 have the same color scales.



(a) 10 db



(b) 300 db



(c) 1500 db

Figure 10: Fitted correlation at temporal lag $\Delta t = 10$ days for the locally stationary 3-month spatio-temporal model with a Gaussian nugget (model 5).